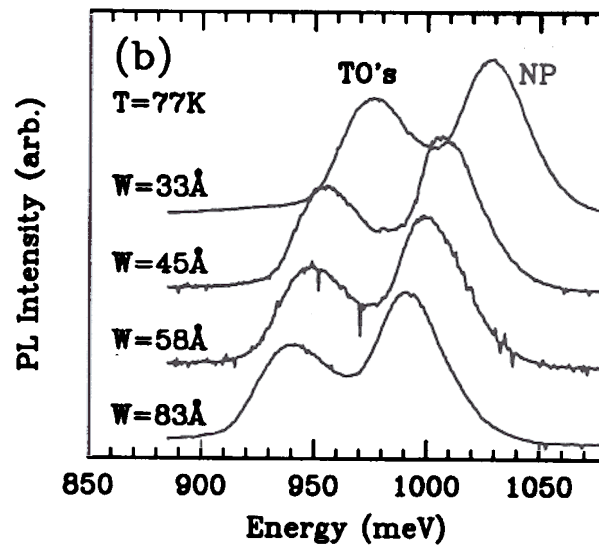


(a)



(b)

Figure 5.5: PL spectra of several  $\text{Si}/\text{Si}_{1-x}\text{Ge}_x/\text{Si}$  SQW samples with different well widths obtained at (a) 4K and (b) 77K.

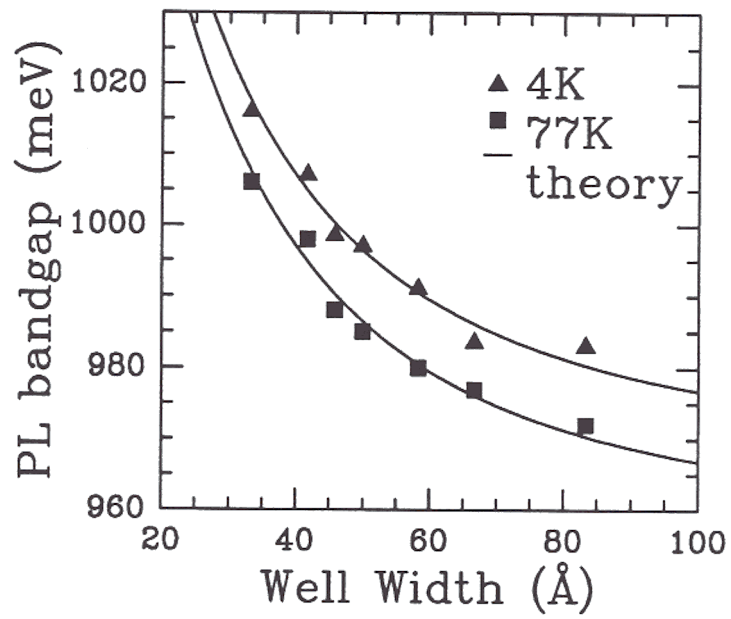


Figure 5.6: PL band gap vs. quantum well width at 4K and 77K. The solid line is from the exact subband calculation. The bulk band gap was fit independently at each temperature.

calculations of the hole ground state energies in the quantum wells which will be discussed next.

### 5.3.3 Effective Mass Calculation

As noted in the previous chapter, the bandgap offset in the Si/strained Si<sub>1-x</sub>Ge<sub>x</sub> system for low  $x$  values is almost entirely in the valence band. Therefore we have focussed on the valence band and neglected the confinement effect in the conduction band in our calculations. Also neglected was any possible variation of exciton binding energy with well width. The quantum confinement effects were then modeled by performing a detailed calculation of the hole subbands in the Si/Si<sub>1-x</sub>Ge<sub>x</sub>/Si quantum wells.

#### Hole Effective-Mass Hamiltonian

The valence band maxima of unstrained Si, Ge, and Si<sub>1-x</sub>Ge<sub>x</sub> alloy correspond to the irreducible representation  $\Gamma_{25}^+$  of the cubic group  $O_h$  when the electron spin is ignored. With the spin included, this 6 dimensional representation reduces to 4-fold  $\Gamma_8^+$  (heavy/light hole band) and 2-fold  $\Gamma_7^+$  (spin-orbit split-off band). For coherently strained Si<sub>1-x</sub>Ge<sub>x</sub> on a (100) silicon substrate, the uniaxial strain component further splits  $\Gamma_8^+$  into two 2-fold bands (heavy hole and light hole). Because of the small spin-orbit splitting (44meV for Si and 290 meV for Ge) it is necessary to work in the full six dimensional space in order to adequately account for the valence band dispersion of the strained Si<sub>1-x</sub>Ge<sub>x</sub> alloy. The construction of the {6×6} hole effective-mass Hamiltonian based on  $\mathbf{k} \cdot \mathbf{p}$  perturbation theory which includes spin-orbit and strain interactions was treated in detail by Bir and Pikus [43]. The total hole effective-mass Hamiltonian consists of four terms:

$$H_{total} = \frac{\hbar^2 \mathbf{k}^2}{2m} + H_{\mathbf{k} \cdot \mathbf{p}} + H_{s-o} + H_{strain} \quad (5.2)$$

where  $\hbar^2\mathbf{k}^2/2m$  is the free-electron term,  $H_{\mathbf{k}\cdot\mathbf{p}}$  is the perturbation from other bands through  $\mathbf{k}\cdot\mathbf{p}$  interactions,  $H_{s-o}$  is the spin-orbit coupling Hamiltonian, and  $H_{strain}$  is the phenomenological strain Hamiltonian.

The strain tensor for strained  $\text{Si}_{1-x}\text{Ge}_x$  on a (100) silicon substrate can be written as:

$$e = \begin{pmatrix} e_{xx} & 0 & 0 \\ 0 & e_{xx} & 0 \\ 0 & 0 & e_{zz} \end{pmatrix} = \frac{2e_{xx} + e_{zz}}{3}I + \frac{e_{zz} - e_{xx}}{3} \begin{pmatrix} -1 & 0 & 0 \\ 0 & -1 & 0 \\ 0 & 0 & 2 \end{pmatrix}$$

where  $I$  is the identity matrix. The three non-vanishing strain components  $e_{xx}$ ,  $e_{yy}$  and  $e_{zz}$  are given by

$$e_{xx} = e_{yy} = \frac{a_{si} - a(x)}{a(x)} \quad (5.4)$$

and

$$e_{zz} = \frac{1 + \sigma}{1 - \sigma} \left( \frac{a(x) - a_{si}}{a_{si}} \right)$$

where  $a(x)$  is the lattice constant of the unstrained  $\text{Si}_{1-x}\text{Ge}_x$  alloy,  $\sigma$  is the Poisson ratio of the alloy, and  $a_{si}$  is the silicon lattice constant. The total strain decomposes into a hydrostatic term and an uniaxial component with the strain axis along the growth direction as shown Equation 5.3. Hydrostatic strain does not change the cubic symmetry of the crystal, and therefore to the lowest order only produces a uniform shift in the valence band energies, The uniaxial component, however, does cause band mixing and splitting and also changes the hole effective masses. The {6

$\times 6$  } uniaxial strain Hamiltonian in the  $|JM_J\rangle$  representation is [44]:

$$H_{\text{strain}} = \begin{pmatrix} |\frac{3}{2}, \frac{3}{2}\rangle & |\frac{3}{2}, \frac{1}{2}\rangle & |\frac{3}{2}, -\frac{1}{2}\rangle & |\frac{3}{2}, -\frac{3}{2}\rangle & |\frac{1}{2}, \frac{1}{2}\rangle & |\frac{1}{2}, -\frac{1}{2}\rangle \\ \epsilon & 0 & 0 & 0 & 0 & 0 \\ 0 & -\epsilon & 0 & 0 & -\sqrt{2}\epsilon & 0 \\ 0 & 0 & -\epsilon & 0 & 0 & \sqrt{2}\epsilon \\ 0 & 0 & 0 & \epsilon & 0 & 0 \\ 0 & -\sqrt{2}\epsilon & 0 & 0 & 0 & 0 \\ 0 & 0 & \sqrt{2}\epsilon & 0 & 0 & 0 \end{pmatrix} \quad (5.6)$$

where

$$\epsilon = \frac{2}{3} D_u (e_{zz} - e_{xx}) \quad (5.7)$$

$D_u$  is the uniaxial strain deformation potential.

In the same representation, the spin-orbit interaction Hamiltonian has a diagonalized form, and reads

$$H_{s-o} = \begin{pmatrix} \Delta/3 & 0 & 0 & 0 & 0 & 0 \\ 0 & \Delta/3 & 0 & 0 & 0 & 0 \\ 0 & 0 & \Delta/3 & 0 & 0 & 0 \\ 0 & 0 & 0 & \Delta/3 & 0 & 0 \\ 0 & 0 & 0 & 0 & -2\Delta/3 & 0 \\ 0 & 0 & 0 & 0 & 0 & -2\Delta/3 \end{pmatrix} \quad (5.8)$$

where  $\Delta$  is the spin-orbit splitting.

The  $\mathbf{k} \cdot \mathbf{p}$  perturbation matrix is slightly more complex. From group and perturbation theories, it can be shown that the matrix on the basis set  $\epsilon_1^+$ ,  $\epsilon_2^+$ , and  $\epsilon_3^+$  (Dresselhaus, Kip, and Kittel's notation [45]) has the form

$$Y = \begin{pmatrix} Lk_x^2 + M(k_y^2 + k_z^2) & Nk_x k_y & Nk_x k_z \\ Nk_x k_y & Lk_y^2 + M(k_x^2 + k_z^2) & Nk_y k_z \\ Nk_x k_z & Nk_y k_z & Lk_z^2 + M(k_x^2 + k_y^2) \end{pmatrix} \quad (5.9)$$

where

$$L = F + 2G, \quad M = H_1 + H_2, \quad N = F - G + H_1 - H_2 \quad (5.10)$$

The parameters  $F$ ,  $G$ ,  $H_1$ , and  $H_2$  first introduced by Dresselhaus, Kip and Kittel [45] correspond to contributions from representation  $\Gamma_2^-$ ,  $\Gamma_{12}^-$ ,  $\Gamma_{15}^-$ , and  $\Gamma_{25}^-$ , respectively, which can perturb the valence band edge  $\Gamma_{25}^+$ .

Expanding this matrix from  $3 \times 3$  to  $6 \times 6$  to include basis functions of two electron spin states, on the basis set  $\{|\epsilon_1^+ \uparrow\rangle, |\epsilon_2^+ \uparrow\rangle, |\epsilon_3^+ \uparrow\rangle, |\epsilon_1^+ \downarrow\rangle, |\epsilon_2^+ \downarrow\rangle, |\epsilon_3^+ \downarrow\rangle\}$  the perturbation matrix becomes, symbolically,

$$H'_{\mathbf{k}\cdot\mathbf{p}} = \begin{pmatrix} Y & 0 \\ 0 & Y \end{pmatrix} \quad (5.11)$$

Through an unitary transformation to the common  $\{Jm_J\}$  representation, we finally obtain the  $\mathbf{k} \cdot \mathbf{p}$  perturbation Hamiltonian

$$H_{\mathbf{k}\cdot\mathbf{p}} = U^{-1} H'_{\mathbf{k}\cdot\mathbf{p}} U \quad (5.12)$$

where the transformation matrix  $U$  is [46],

$$U = \begin{pmatrix} -1/\sqrt{2} & 0 & 1/\sqrt{6} & 0 & 0 & 1/\sqrt{3} \\ -i/\sqrt{2} & 0 & -i/\sqrt{6} & 0 & 0 & -i/\sqrt{3} \\ 0 & 2/\sqrt{6} & 0 & 0 & -1/\sqrt{3} & 0 \\ 0 & -1/\sqrt{6} & 0 & -1/\sqrt{2} & -1/\sqrt{3} & 0 \\ 0 & -i/\sqrt{6} & 0 & i/\sqrt{2} & -i/\sqrt{3} & 0 \\ 0 & 0 & 2/\sqrt{6} & 0 & 0 & -1/\sqrt{3} \end{pmatrix} \quad (5.13)$$

The difference between Equation 5.13 and that given by Kane is due to the different ordering of the basis functions.

While values of deformation potentials and valence band effective mass parameters [47] are known to high accuracy for pure Si and Ge, for  $\text{Si}_{1-x}\text{Ge}_x$  alloys one is forced to resort to interpolations to obtain these parameters needed in band structure calculations. For the uniaxial deformation potential  $D_u$ , spin-orbit splitting  $\Delta$ ,

	$\gamma_1$	$\gamma_2$	$\gamma_3$	$\kappa$	$q$	$D_v(\text{eV})$	$\Delta(\text{eV})$	$\sigma$	$a_0(\text{\AA})$
Si	4.285	0.339	1.446	-0.26	0.01	2.04	0.044	0.280	5.43
Ge	13.38	4.239	5.69	3.41	0.07	3.81	0.290	0.273	5.65

Table 5.1: Parameters used in valence band structure calculations of strained  $\text{Si}_{1-x}\text{Ge}_x$  alloy. The units of  $\gamma_1$ ,  $\gamma_2$ ,  $\gamma_3$ ,  $\kappa$ , and  $q$  are  $\frac{\hbar^2}{2m}$ .

Poisson ratio  $\sigma$ , and unit cell volume  $a_0^3$ , we assume linear variation on composition following People [12]. For the Luttinger valence band parameters of the SiGe alloy, we follow Braunstein [48] assuming linear variation of  $1/F$ ,  $1/G$ ,  $1/H_1$ , and  $1/H_2$  with composition. Tabulated in Table 5.1 are values of all the parameters used in our calculation, which are from Ref.[12, 49, 50].

For any given crystal momentum  $\mathbf{k}$ , the total Hamiltonian ( a  $6 \times 6$  matrix ) can be constructed and solved numerically. While the six eigenvalues give the energies at that particular  $\mathbf{k}$  for all three doubly-degenerate bands (heavy hole, light hole, and spin-orbit split-off band), the eigenvectors give the wave-functions in terms of those basis function. The valence band dispersion calculated using this  $6 \times 6$  effective-mass Hamiltonian has been reported by Manku and Nathan [51].

### Quantum Well Subband Calculation

For a  $\text{Si}/\text{Si}_{1-x}\text{Ge}_x/\text{Si}$  quantum well, assuming flat-band condition in all three layers, the hole effective-mass Hamiltonian can be constructed in each layer as discussed in the previous section. To calculate the quantized energy levels in the quantum well, we solve the total effective-mass equations with proper boundary conditions using a modified version of the approach suggested by Wessel and Altarelli [52].

Assuming that the normal to the interfaces of the quantum well is the  $z$  direction,  $k_x$  and  $k_y$  remain good quantum numbers because of the in-plane translational symmetry. For each energy  $E$  and in-plane wave vector  $\mathbf{k}_{\parallel}$  the bulk secular equation in each layer gives six values of  $k_z$ , which are denoted  $\pm k_h$ ,  $\pm k_l$ , and  $\pm k_s$ , and

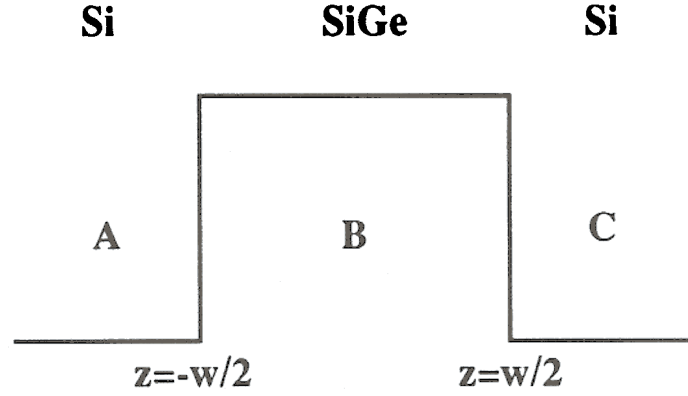


Figure 5.7: Schematic valence band diagram of a Si/Si<sub>1-x</sub>Ge<sub>x</sub>/Si quantum well.

twelve eigenvectors, which are denoted  $h_1(\pm k_h)$ ,  $h_2(\pm k_h)$ ,  $l_1(\pm k_l)$ ,  $l_2(\pm k_l)$ ,  $s_1(\pm k_s)$ , and  $h_2(\pm k_s)$ . The general solution in each layer is a linear combination of these eigenvectors, e.g., in the Si<sub>1-x</sub>Ge<sub>x</sub> well (Figure 5.7):

$$\begin{aligned}
 F(\mathbf{r}) = & [b_1 h_1(+k_h) e^{ik_h z} + b_2 h_2(+k_h) e^{ik_h z} \\
 & + b_3 l_1(+k_l) e^{ik_l z} + b_4 l_2(+k_l) e^{ik_l z} \\
 & + b_5 s_1(+k_s) e^{ik_s z} + b_6 s_2(+k_s) e^{ik_s z} \\
 & + b_7 h_1(+k_h) e^{-k_h z} + b_8 h_2(+k_h) e^{-k_h z} \\
 & + b_9 l_1(+k_l) e^{-ik_l z} + b_{10} l_2(+k_l) e^{-ik_l z} \\
 & + b_{11} s_1(+k_s) e^{-k_s z} + b_{12} s_2(+k_s) e^{-k_s z}] e^{i(k_x x + k_y y)} \quad (5.14)
 \end{aligned}$$

At each interface, from the boundary conditions we get an equation relating the amplitudes on two sides of the interface, e.g., at  $z = -W/2$  (see Figure 5.7)

$$M_1 \mathbf{a} = M_2 \mathbf{b} \quad (5.15)$$

and at  $z = W/2$

$$M_3 \mathbf{b} = M_4 \mathbf{c} \quad (5.16)$$

where  $M_2$  and  $M_3$  are  $12 \times 12$  matrices which contain the coefficients of amplitudes

$b_i$  in Eqn. 5.14. From Eqn. 5.15 and Eqn. 5.16 we get

$$\mathbf{a} = \mathbf{M}_1^{-1} \mathbf{M}_2 \mathbf{M}_3^{-1} \mathbf{M}_4 \mathbf{c} = \mathbf{M} \mathbf{c} \quad (5.17)$$

where  $\mathbf{M}$  is the total transfer matrix, which directly relates the amplitudes on one side of the quantum well to those on the other side, and is of order 12.

For a stationary state, the wave-function at infinity must not diverge. This condition requires that the amplitudes of the six diverging wave-functions on each side must be zero, and Equation 5.17 becomes

$$\begin{pmatrix} 0 \\ \vdots \\ 0 \\ a_7 \\ \vdots \\ a_{12} \end{pmatrix} = \mathbf{M} \begin{pmatrix} c_1 \\ \vdots \\ c_6 \\ 0 \\ \vdots \\ 0 \end{pmatrix} = \begin{pmatrix} \mathbf{M}_{11} & \mathbf{M}_{12} \\ \mathbf{M}_{21} & \mathbf{M}_{22} \end{pmatrix} \begin{pmatrix} c_1 \\ \vdots \\ c_6 \\ 0 \\ \vdots \\ 0 \end{pmatrix} \quad (5.18)$$

In order to have a nontrivial solution to Eqn. 5.18, the necessary and sufficient condition is that the determinant of the  $6 \times 6$  submatrix  $\mathbf{M}_{11}$  vanish. For a given in-plane wave vector  $\mathbf{k}_{\parallel}$ , if we plot this determinant as a function of energy  $E$ , stationary states will correspond to the points of zero determinant. As an example, for a strained Si/Si<sub>0.80</sub>Ge<sub>0.20</sub>/Si quantum well, at  $\mathbf{k}_{\parallel} = 0$  the calculated  $|\mathbf{M}_{11}|$  is plotted versus energy in Figure 5.8 for both a 50Å well and a 100Å well. In the 50Å well, the first sharp dip in the determinant at  $E=30$  meV corresponds to the ground state of the heavy hole (HH<sub>0</sub>) in the quantum well, and the second dip at 65 meV corresponds to the light hole ground state (LH<sub>0</sub>), etc. Using this technique, the dispersion relation of all hole subbands in the quantum well can be mapped out.

By solving the effective-mass equations using the technique described above, we calculated the hole energy levels in a Si/Si<sub>0.80</sub>Ge<sub>0.20</sub>/Si quantum well as functions of the well width. As can be seen in Fig. 5.9, the lowest energy subband in the quantum

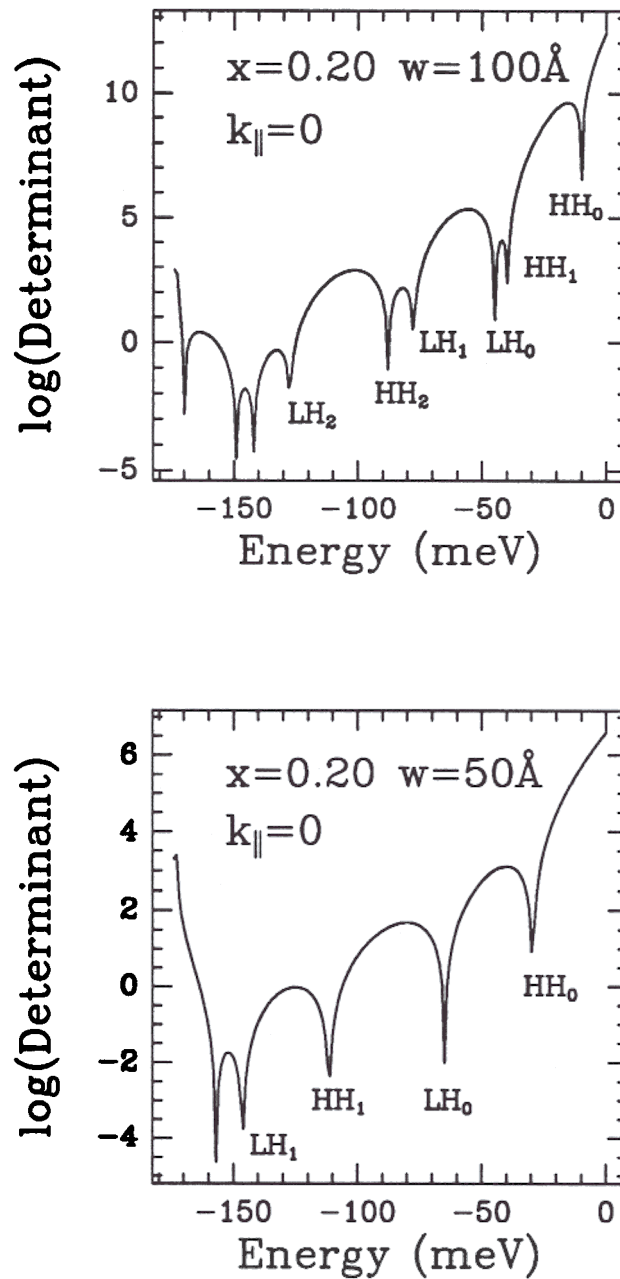


Figure 5.8: Plots of the determinant vs. energy for a 100 Å and 50 Å  $\text{Si}/\text{Si}_{0.80}\text{Ge}_{0.20}/\text{Si}$  quantum well. The position of the sharp dips in the plot correspond to energies of the stationary states associated with the quantum wells.

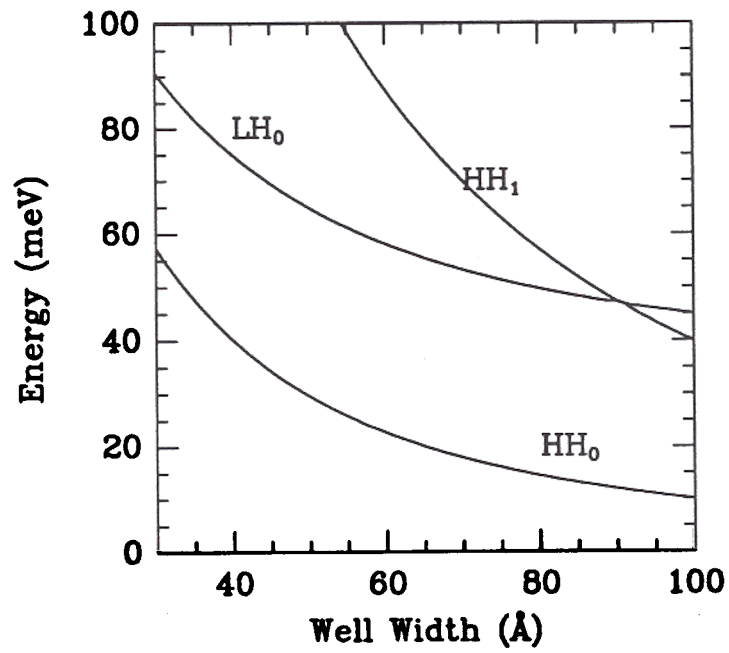


Figure 5.9: Well width dependent quantum confinement energies for several subbands in  $\text{Si}/\text{Si}_{0.80}\text{Ge}_{0.20}/\text{Si}$  quantum wells.

well is the heavy hole band  $\text{HH}_0$ . Photoexcited holes will tend to relax to the heavy hole ground states, and the photoluminescence energy should move with  $\text{HH}_0$  as the quantum well width changes. Therefore, we compare the well width dependent heavy hole ground state energy with the experimentally observed PL shifts. (Figure 5.6) Excellent agreement was achieved between the observed shifts in PL bandgap and the calculated well width dependency of confinement energy. The only adjustable parameter was the absolute value of the bulk bandgap.

As a final note, because the heavy band at zero in-plane wave vector ( $k_{\parallel} = 0$ ) is not coupled with light hole or split-off bands, its dispersion in the  $z$  direction is purely parabolic, and a simple effective mass model can be applied to calculate the heavy hole levels in a quantum well. By interpolation from band parameters of Si and Ge, the  $z$ -direction heavy hole effective mass of strained  $\text{Si}_{1-x}\text{Ge}_x$  can be expressed as  $m_z = 0.278 - 0.07x$ . In any other case, the exact calculation is necessary.

### 5.3.4 Conclusion

In summary we have reported the first observation of the quantum confinement shift of band-edge photoluminescence in Si/strained  $\text{Si}_{1-x}\text{Ge}_x$ /Si quantum wells. Good agreement is found between experiment and a theoretical quantum well subband calculation using the  $6 \times 6$  Luttinger-Kohn effective-mass Hamiltonian which includes both strain and spin-orbit interactions.

# Silicide/Si<sub>1-x</sub>Ge<sub>x</sub> Long-wavelength Infrared Detectors

In this chapter, the development of Pd<sub>2</sub>Si/Si<sub>1-x</sub>Ge<sub>x</sub> and PtSi/Si<sub>1-x</sub>Ge<sub>x</sub> Schottky-barrier infrared detectors is discussed. It is demonstrated that strained Si<sub>1-x</sub>Ge<sub>x</sub> can be used to tune the cut-off wavelength of silicide Schottky-barrier detectors. Good photo-response as well as near-ideal reverse leakage have been achieved in these devices.

## 6.1 Introduction

### 6.1.1 Thermal Radiation and Imaging

From Planck blackbody radiation theory, every object whose temperature is not absolute zero emits “thermal radiation”, and the spectral radiance of a blackbody is given by

$$F(T, \lambda) = \frac{2hc^2}{\lambda^5} \frac{1}{e^{hc/\lambda kT} - 1} \quad [W/cm^2 SR/\mu m] \quad (6.1)$$

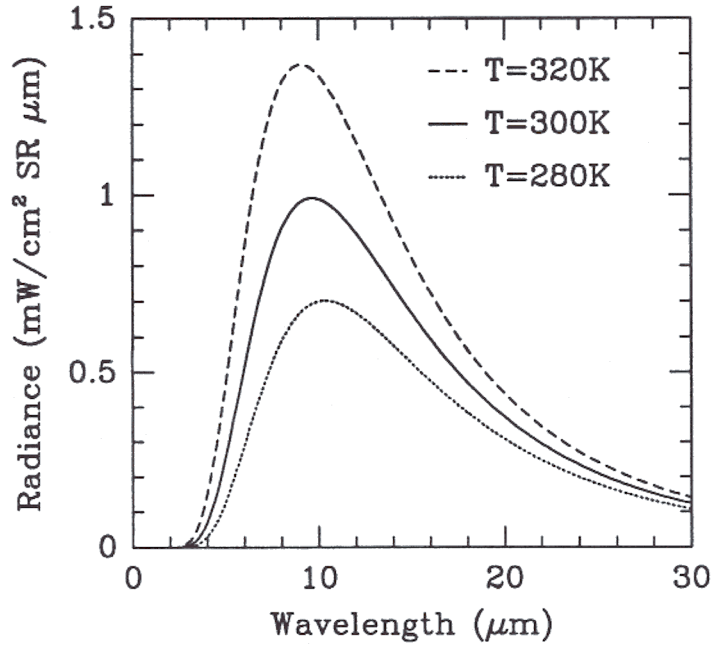


Figure 6.1: Spectral radiance of a blackbody at temperatures near 300K.

$$F(T, \lambda) = \frac{2c}{\lambda^4} \frac{1}{e^{hc/\lambda kT} - 1} \left[ \text{photons}/\text{cm}^2 \text{SR}/\mu\text{m} \right] \quad (6.2)$$

where  $T$  is the blackbody temperature,  $\lambda$  the wavelength,  $h$  Planck's constant,  $c$  the speed of light in vacuum,  $k$  the Boltzmann constant, and  $SR$  stands for steradians. The spectral radiance of a blackbody at three different temperatures is plotted in Figure 6.1. It is clear that most of the energy thermally emitted from objects at terrestrial temperatures is in the long-wavelength infrared.

Thermal imaging systems extend human vision into the far infrared by making visible the thermal radiation naturally emitted by objects of finite temperature. For many applications it is very desirable to have detectors sensitive to radiation in the 8 to 12  $\mu\text{m}$  wavelength range, which is so called "Long-Wavelength Infrared" (LW-IR). There are two reasons which make the 8–12 $\mu\text{m}$  band of particular importance.

First, this wavelength range corresponds to the emission peak in the thermal radiation spectrum from an object at terrestrial temperatures (Figure 6.1). Second, there is an atmospheric transmission window [53] in this band which allows signal detection over comparatively long distances.

There are several major competing technologies for long-wavelength infrared imaging applications. One is based on narrow bandgap semiconductors such as Hg<sub>1-x</sub>Cd<sub>x</sub>Te. Another is based on inter-subband transitions in GaAs/AlGaAs quantum-wells. The advantage of these two approaches is that high quantum efficiency can be achieved. On the other hand, fabricating large focal-plane-arrays is very difficult due to uniformity problems, and the integration of detector arrays with read-out circuitry also poses a big challenge. The other approach is silicon-based Schottky-barrier Focal-Plane-Array (FPA) technology. Even though they have lower quantum efficiencies, Schottky-barrier detectors are compatible with silicon process technology, and they can be easily integrated with CCD or MOS read-out circuitry. At present very large (480×640) Schottky-barrier FPA's are available which offer very high resolution and sensitivity.

### 6.1.2 Silicide/Silicon Schottky Barrier Detectors

Silicide/Silicon Schottky-barrier infrared image sensor technology has been developed to such an advanced level that very large focal plane arrays (with > 10<sup>5</sup> detector elements) can be fabricated. Detailed treatment of this subject can be found in many original as well as review articles [54, 55, 56, 57, 58]. Here, a very simple picture of the construction and operation of a silicide Schottky-barrier infrared detector will be given.

The construction of a high-performance PtSi/Si Schottky-barrier detector is illustrated in Figure 6.2 [59]. Light is typically incident on the wafer backside, where

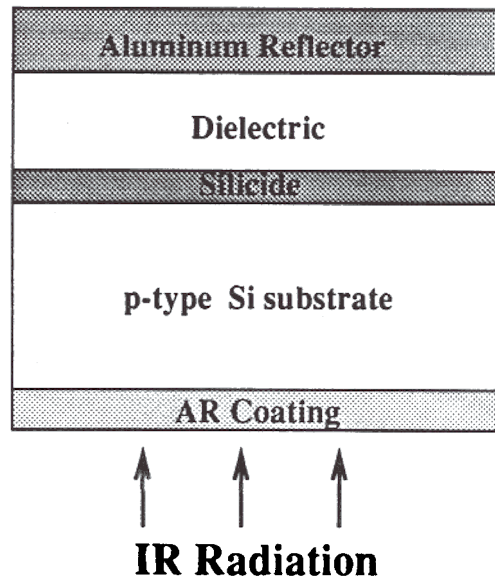


Figure 6.2: Schottky-barrier detector with AR coating and optical cavity.

an anti-reflection coating increases the coupling of infrared radiation into the detector by about 30%. The photoresponse of the Schottky-barrier detectors results from the injection of photoexcited hot holes from the silicide film into the silicon substrate (Figure 6.3). The optical cavity formed by the top aluminum reflector and the silicide film enhances optical absorption as the result of multiple passes of the light through the silicide film. To have any photocurrent, holes must be able to gain enough energy

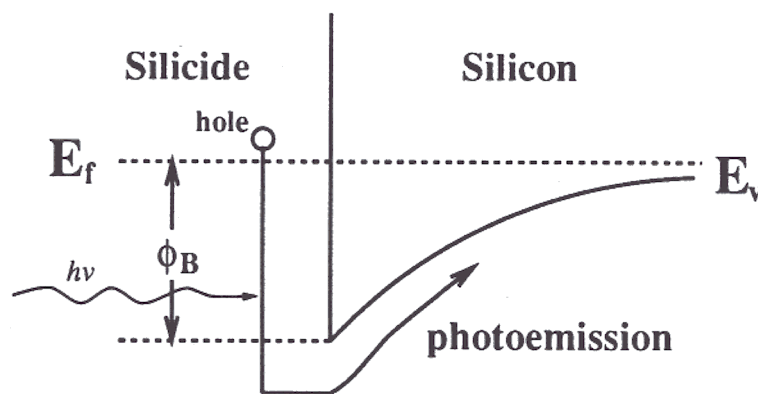


Figure 6.3: Schematic band diagram of a Schottky-barrier detector.

from the incoming photons to overcome the barrier at the interface, which means the photon energy has to be larger than the Schottky-barrier height (neglecting any holes below the Fermi level due to finite temperature). The cutoff wavelength of such a detector is given by

$$\lambda_c = \frac{1.24}{\phi_B(\text{eV})} \mu\text{m} \quad (6.3)$$

where  $\phi_B$  is the Schottky-barrier height.

While the prediction of its cutoff wavelength is straightforward, the spectral response of a Schottky-barrier detector is a much more complex problem. In fact, it is so difficult to develop a complete and rigorous treatment that the most successful and most widely used theory today is still the general one which was developed by Fowler back in 1931 [60]. At the heart of his analysis lies the hypothesis that *“the photoelectric sensitivity or number of electrons emitted per quantum of light absorbed is to a first approximation proportional to the number of electrons per unit volume of the metal whose kinetic energy normal to the surface augmented by  $h\nu$  is sufficient to overcome the potential step at the surface”*.

Based on this hypothesis, it can be derived that the external quantum efficiency  $Y$  of a Schottky-barrier detector is approximately given by [60]

$$Y = C_1(h\nu - \phi_B)^2 \quad (6.4)$$

where  $C_1$  is the so-called quantum efficiency coefficient. According to this Fowler theory, the square root of the quantum efficiency  $Y$  plotted versus the photo energy  $h\nu$  (Fowler plot) near the threshold should be a straight line. By linearly extrapolating to zero response, an accurate Schottky-barrier height can be obtained.

### 6.1.3 $\text{Si}_{1-x}\text{Ge}_x$ for Infrared Detectors

One major problem of silicide/silicon Schottky-barrier detectors is that the barrier height (hence the cut-off wavelength) is determined by the metal used, and very

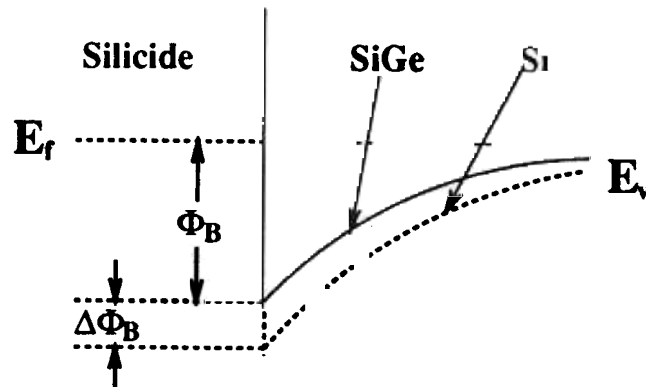


Figure 6.4: Schottky-barrier height reduction by Si<sub>1-x</sub>Ge<sub>x</sub> alloy

little adjustment can be made by changing the doping level in the silicon substrate. While the palladium-silicide Schottky-barrier (Pd<sub>2</sub>Si/Si) has a barrier height of about 0.41eV and a cutoff wavelength of 3.0 $\mu$ m, the platinum-silicide (PtSi/Si) has a cutoff wavelength of about 5 $\mu$ m. In order to go beyond 10 $\mu$ m, Iridium-silicide (IrSi) detectors are currently being developed [61, 62]. Among the three, the PtSi/Si infrared detector is the most advanced. The state-of-the-art silicide infrared focal plane arrays are based on platinum because of its high quantum efficiency coefficient, high uniformity, and ease of integration. It will be, therefore, advantageous to extend the cutoff wavelength of the PtSi detector to beyond 10 $\mu$ m for long-wavelength applications.

As shown in an earlier chapter of this thesis, a strained Si<sub>1-x</sub>Ge<sub>x</sub> alloy on (100) silicon has a large valence band offset to Si. Based on this fact, two different schemes have been proposed to make long-wavelength infrared detectors based on Si<sub>1-x</sub>Ge<sub>x</sub>. In 1990, Lin et al. first successfully demonstrated a novel Si<sub>1-x</sub>Ge<sub>x</sub>/Si heterojunction internal photoemission (HIP) long-wavelength infrared detectors [35]. The HIP detectors are based on photo-injection of hot holes from heavily doped p-type Si<sub>1-x</sub>Ge<sub>x</sub> into the silicon substrate as shown in Figure 4.7. A year before that, in 1989, Kanaya et al [63] proposed using Si<sub>1-x</sub>Ge<sub>x</sub> alloy to reduce the Schottky-barrier heights to silicides (Figure 6.4). Unfortunately, neither optical response nor reverse leakage data

were reported from their devices. They estimated the Schottky-barrier heights for both Pd and Pt devices from their forward I-V characteristics at 77K, which were far from ideal, with their ideality factors in the range of 1.2 to 1.3.

In this thesis, by employing a thin silicon sacrificial layer for silicide formation on Si<sub>1-x</sub>Ge<sub>x</sub>, operation of silicide/Si<sub>1-x</sub>Ge<sub>x</sub> infrared detectors has been demonstrated for the first time.

## 6.2 Silicide/Si<sub>1-x</sub>Ge<sub>x</sub> Schottky Barriers

In this section, the physics of silicide Schottky-barrier formation will first be reviewed. Based on theoretical analysis, the concept of a silicon sacrificial layer is introduced. It is then experimentally demonstrated that the thin silicon sacrificial layer indeed eliminates Fermi level pinning which will result from segregation of Ge when metal directly reacts with Si<sub>1-x</sub>Ge<sub>x</sub> alloy layer.

### 6.2.1 Formation of Schottky Barriers

#### The Schottky-Mott model

When a metal comes into contact with a semiconductor at equilibrium, the Fermi levels in the metal and the semiconductor line up due to charge transfer across the junction. Assuming that the surface dipole contributions to the metal work function  $\phi_m$  and semiconductor electron affinity  $\chi_s$  do not change when the metal and semiconductor are brought into contact, and that there are no localized states at the interface, the Schottky barrier height for a p-type semiconductor measured relative to the Fermi level is given by

$$\phi_B = E_g + \chi_s - \phi_m \quad (6.5)$$

where  $E_g$  is the band gap of the semiconductor (Figure 6.5). Equation 6.5 is often

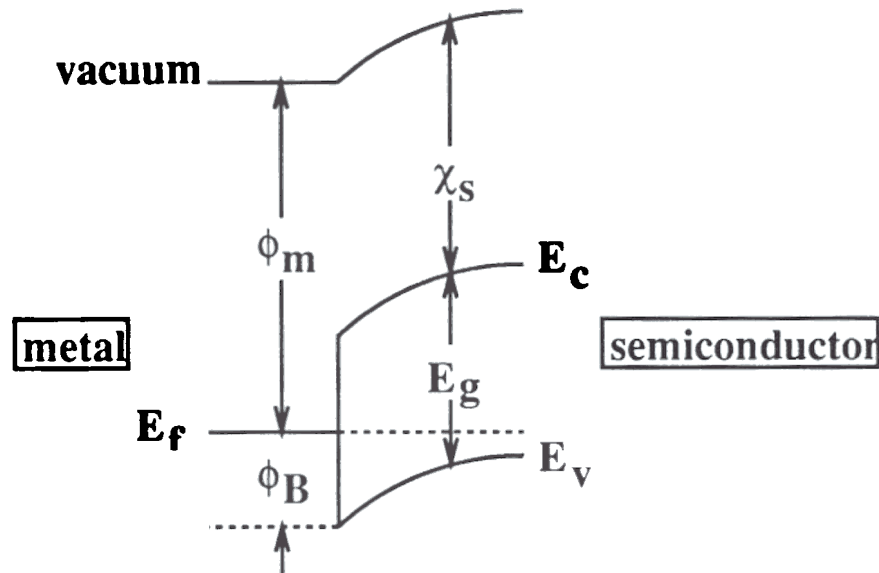


Figure 6.5: Schottky barrier to a p-type semiconductor.

referred to as the Schottky-Mott limit

### Interface states and the Bardeen model

Unfortunately, reality is much more unpredictable than what Equation 6.5 would suggest. Experimentally, the barrier height is found to be almost independent of the metal work function under certain circumstances. In explaining the discrepancy, a model was put forward by Bardeen, who suggested the Fermi level pinning effect of interface states [64].

To see how interface states can affect the barrier height, suppose that the metal and semiconductor remain separated by a thin interfacial insulating layer as shown in Fig. 6.6 and that there is a distribution of interface states present on the semiconductor side which can be characterized by a charge neutrality level  $\phi_0$ . In the absence of interface states, the positive charge  $Q_m$  on the surface of the metal must be equal and opposite to the negative charge  $Q_a$  in the semiconductor due to uncompensated acceptors in the depletion region near the interface. In the presence of

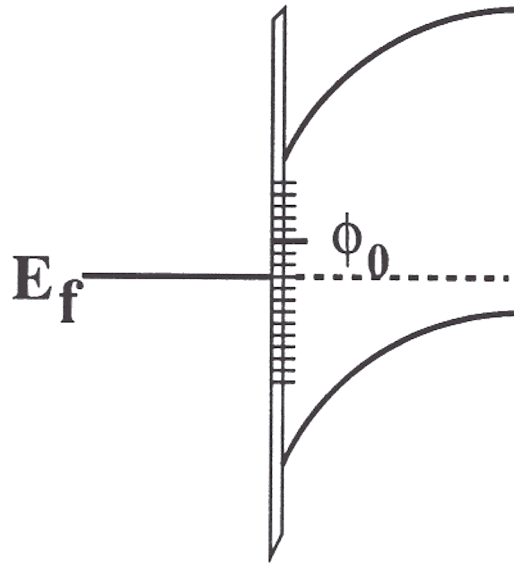


Figure 6.6: Schematic band diagram of Schottky-barrier with interface states.

interface states, the total charge neutrality condition is given by  $Q_m + Q_{ss} + Q_a = 0$ , where  $Q_{ss}$  is the charge due to the interface states. The occupancy of the interface states is determined by the Fermi level  $E_F$ . If the interface charge neutral level  $\phi_0$  lies above the the  $E_F$ , there will be a net positive charge due to the interface states and  $Q_a$  must therefore be more negative than if the interface states were absent. This means that the barrier height will be increased. Similarly, it can be shown that if  $\phi_0$  is below the Fermi level  $E_f$ , a small barrier height will result.

The interface states therefore tend to pull the Fermi level  $E_F$  toward its charge neutral level  $\phi_0$ . If the density of states near  $\phi_0$  at the interface is sufficiently high, the Fermi level will be pinned at the  $\phi_0$ , in which case the barrier height will be given by

$$\phi_B = \phi_0 - E_v \quad (6.6)$$

where  $E_v$  is the valence band edge of the semiconductor. This is usually referred to as the Bardeen limit.

### Intimate contacts and the “defect model”

Silicide/Si contacts are often formed by physical deposition of a thin film of metal onto a very clean silicon surface, followed by a subsequent sintering step at elevated temperatures (200 to 600 °C), during which the silicide compound is formed as the result of chemical reaction between the deposited metal film and the silicon substrate. Two particular silicides of interest here are palladium-silicide (Pd<sub>2</sub>Si) and platinum-silicide (PtSi) because of their application in Schottky-barrier infrared detectors.

It is understood that the metal-silicon reaction proceeds by metal diffusion through the silicide film and subsequent reaction with the silicon at the silicide/Si interface[65]. Since a layer of silicon at the top surface was consumed during the reaction, an ultra-clean and highly reproducible silicide/Si intimate contact can be formed, provided the starting silicon surface is free from contamination. An intimate contact is usually referred to as a metal-semiconductor contact free from a thin interfacial insulating layer.

Even in the case of a clean intimate contact, the Schottky-Mott limit still does not always hold true. The termination of the bulk periodic potential of a semiconductor at its surface leads to surface states whose wave-functions decay exponentially into the bulk. In the presence of a metal on the surface, as in the case of a metal-semiconductor contact, these surface states will be replaced by metal-induced gap states (MIGS). These MIGS are associated with the wave function tails of the conduction electrons in the metal which tunnel into the semiconductor at the interface. These MIGS affect the barrier height in the same way as the interface states do in the Bardeen model. For an interface which is imperfect, defects such as interstitials or vacancies may lead to additional localized states at the interface. These defect states may also affect the barrier height or even pin the Fermi level.

### Barrier height engineering with Si<sub>1-x</sub>Ge<sub>x</sub>

Strained Si<sub>1-x</sub>Ge<sub>x</sub> alloys have smaller bandgaps than Si, with almost all of the bandgap reduction occurring as a valence band offset, which implies by definition that  $\chi_s + E_g$  is smaller in strained Si<sub>1-x</sub>Ge<sub>x</sub> than in Si. It is expected from the Schottky model (Eqn. 6.5) that Si<sub>1-x</sub>Ge<sub>x</sub> will have a smaller Schottky barrier height to silicide than does pure Si because of its smaller  $\chi_s + E_g$ . This would allow us make infrared detectors with a cutoff tunable by adjusting the Ge fraction.

In many cases the Schottky-model fails to predict the right barrier heights because it does not take into account of the effects of interface states which are always present. These interface states can pin the Fermi level if their density is sufficiently high. In an interfacial reaction study of Pt and Pd with Si<sub>1-x</sub>Ge<sub>x</sub> alloys by Liou et al. [66], it has been shown that the metals tend to react with Si preferentially, causing Ge segregation at the interfaces and Fermi level pinning near mid-gap. The exact nature of the defects was not known, however. In order to make silicide/Si<sub>1-x</sub>Ge<sub>x</sub> long-wavelength infrared detectors, the Ge segregation must be eliminated. A straightforward way to avoid this problem is to use a silicon sacrificial layer on top of the Si<sub>1-x</sub>Ge<sub>x</sub> alloy layer for the metal reaction. The deposited metal reacts with the pure silicon sacrificial layer rather than with Si<sub>1-x</sub>Ge<sub>x</sub> alloy, and a true silicide (without Ge) contact can be formed (Fig. 6.7).

It is clear from both silicide work function and Ge segregation considerations that a silicon sacrificial layer is the choice for silicide formation. The next section will show experimentally that the silicon sacrificial layer does eliminate Fermi level pinning, and, with the sacrificial layer, reduced Schottky-barrier heights can be obtained for silicide/Si<sub>1-x</sub>Ge<sub>x</sub> contacts.

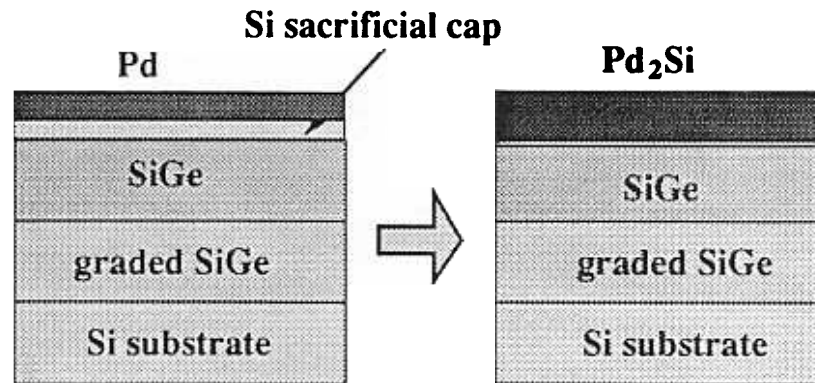


Figure 6.7: Silicon sacrificial layer reacts with deposited metal forming a true silicide (without Ge) on Si<sub>1-x</sub>Ge<sub>x</sub> alloy.

## 6.2.2 Silicon Sacrificial Layer

### Sample structure and processing

In order to examine the effects of a silicon sacrificial layer, two very similar samples were grown (#1058 & #1080). They both started with a lightly doped p-type substrate. After a thin silicon buffer layer, a graded Si<sub>1-y</sub>Ge<sub>y</sub> ( $y : 0 \rightarrow 0.20$ ) alloy layer was grown followed by a constant composition Si<sub>0.80</sub>Ge<sub>0.20</sub> layer. While one sample (#1058) had a thin (100Å) silicon cap layer on top of the Si<sub>0.80</sub>Ge<sub>0.20</sub> alloy, the other sample (#1080) did not. The purpose of the graded Si<sub>1-y</sub>Ge<sub>y</sub> layer was to eliminate the parasitic valence band barrier which could stop hole transport at an abrupt Si<sub>0.80</sub>Ge<sub>0.20</sub>/substrate Si interface (Figure 6.8) From our experience, the Si<sub>1-x</sub>Ge<sub>x</sub> layers were expected to be fully strained. The exact growth sequence (times/flows/temperatures) of a typical sample (#1058) is given in Appendix A.

After the epitaxial growth, these two samples and an all-silicon control wafer were processed in an identical sequence. First, a plasma-enhanced CVD oxide layer was deposited on top of the samples at 350°C. Then, windows were opened in this oxide layer by wet chemical etching exposing the Si (or Si<sub>1-x</sub>Ge<sub>x</sub>) layer underneath. After a short dip in HF : H<sub>2</sub>O (1:50), the samples were immediately loaded into

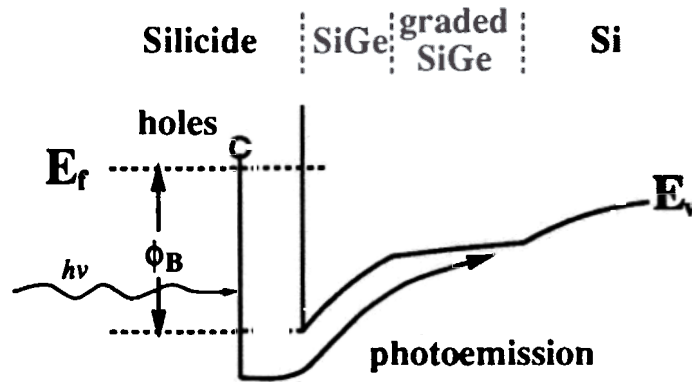
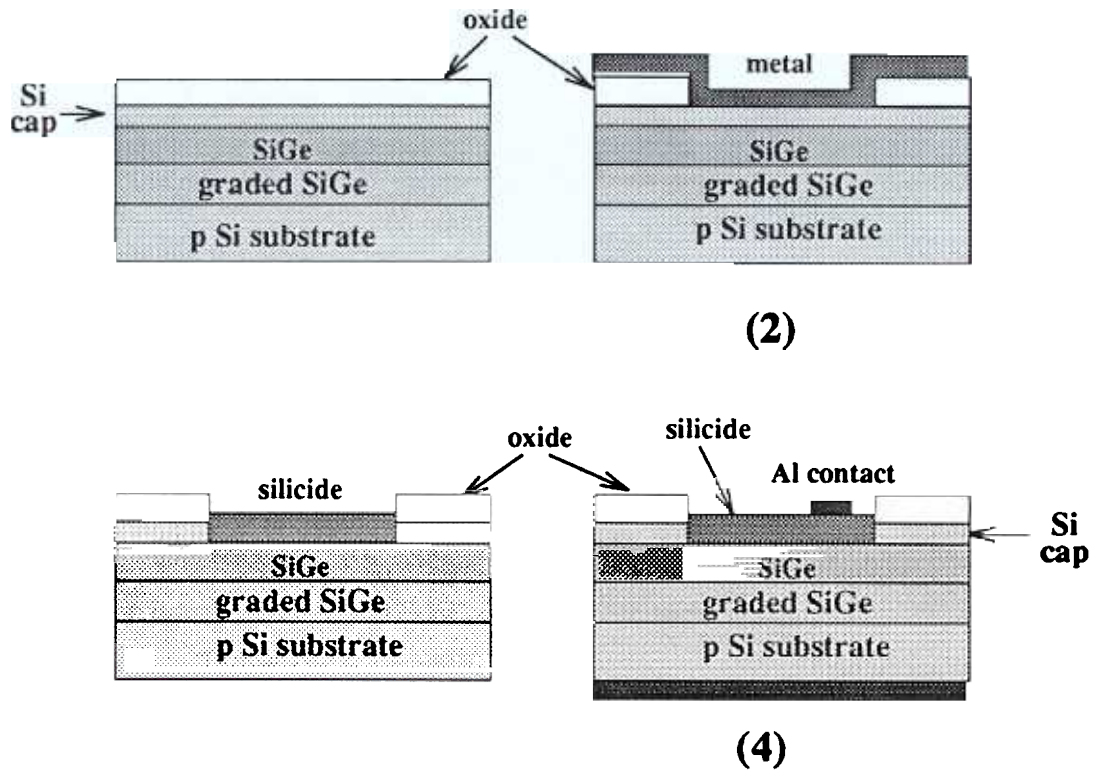


Figure 6.8: Schematic band diagram of a silicide/Si<sub>1-x</sub>Ge<sub>x</sub> detector

an e-beam evaporator where a layer of Pd ( $\sim 150\text{\AA}$ ) was deposited. The samples (with evaporated Pd) were annealed at  $200^\circ\text{C}$  for ten minutes in forming gas (10% H<sub>2</sub> and 90% N<sub>2</sub>). Inside the oxide windows Pd reacted with the underlying Si (or Si<sub>1-x</sub>Ge<sub>x</sub>) forming palladium silicide, but the metal on top of the oxide film remained unreacted and was subsequently etched away selectively in a KI : I<sub>2</sub> : H<sub>2</sub>O solution, leaving a silicide/Si<sub>1-x</sub>Ge<sub>x</sub> contact in the windows. Note that in the silicon cap case, the expected silicide phase would be Pd<sub>2</sub>Si [65], forming  $\sim 200\text{\AA}$  of Pd<sub>2</sub>Si and consuming  $\sim 102\text{\AA}$  of silicon. The precise composition created by the interaction of Pd with Si<sub>0.8</sub>Ge<sub>0.2</sub> is unknown [66]. Finally, aluminum was used for both silicide and substrate contacts. There was no AR coating or optical cavity as in Fig. 6.2, and all measurements were performed using front side illumination. The process sequence is shown schematically in Figure 6.9

### Photo-response characterization

To measure the Schottky-barrier heights, we used the internal photoemission technique, upon which the operation of Schottky-barrier infrared detectors is based. The samples were wire-bonded and mounted on the cold head of a liquid nitrogen cooled dewar which has a Ge window allowing exposure of the device to infrared radiation



1. epitaxial growth and oxide deposition
2. open windows by wet-etching and metal deposition
3. heat treatment and selective removal of unreacted metal
4. aluminum contact metalization

Figure 6.9: Silicide/Si<sub>1-x</sub>Ge<sub>x</sub> detector process flow

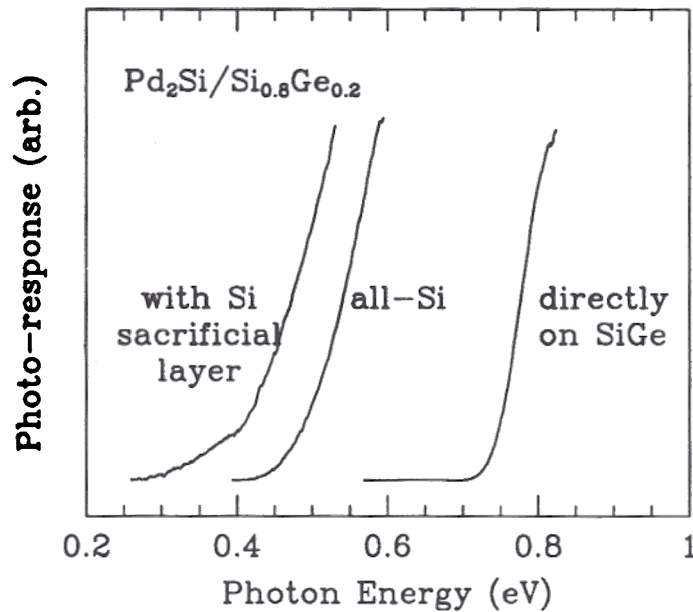


Figure 6.10: Spectral responses of three different samples indicating that the silicon sacrificial layer eliminated Ge segregation-induced Fermi level pinning, resulting in a lower silicide/Si<sub>1-x</sub>Ge<sub>x</sub> Schottky-barrier height.

The photoresponse of the device was measured in a Fourier Transform Infrared spectrometer (FT-IR). The instrument was calibrated with a pyroelectric detector with a known spectral response. The measured results for all three samples are shown in Figure 6.10. All three devices show characteristic Schottky-barrier spectral response with a well defined cutoff photon energy which gives corresponding barrier height. For the all-silicon control device, we obtained a cutoff of 420meV which agrees well with the established value of the p-type Pd<sub>2</sub>Si/Si Schottky-barrier height. For sample #1080, which did not have a silicon sacrificial layer, the measured barrier height was 700meV, corresponding to an *increase* of about 300meV compared to the Pd<sub>2</sub>Si/Si contact, which is exactly the opposite of what we wanted. It is most likely due to

Ge segregation during Pd-Si<sub>1-x</sub>Ge<sub>x</sub> reaction and consequent Fermi level pinning [66]. Sample #1058, which did have a silicon sacrificial layer, on the other hand, had a barrier height of 260meV, corresponding to a reduction of 160meV. This experiment clearly demonstrated that a silicon sacrificial layer is effective in eliminating Ge segregation and Fermi level pinning. In the experiments discussed in the rest of the thesis, unless explicitly so indicated, all devices were fabricated by employing a silicon sacrificial layer for metal reaction.

### 6.2.3 A Modified Fowler Theory

It should be noted that due to unavoidable variations in the silicon cap layer and deposited metal thicknesses, it is possible that a very thin layer of excess silicon was left in some devices, or that some Si<sub>1-x</sub>Ge<sub>x</sub> was consumed. If excess sacrificial silicon is left unconsumed in our detector structure, an interfacial barrier due to the Si will face the holes as they attempt to reach the Si<sub>1-x</sub>Ge<sub>x</sub>. Fig. 6.11 is a schematic band diagram of such a device. There are two barrier heights involved in this structure: the parasitic barrier height due to the thin Si layer ( $\phi_{Si}$ ) and the desired barrier height due to the underlying Si<sub>1-x</sub>Ge<sub>x</sub> alloy ( $\phi_{SiGe}$ ). Because of the narrow width of the Si barrier, photoexcited holes will have a finite probability of tunneling through it even if their energy normal to the surface lies between  $\phi_{Si}$  and  $\phi_{SiGe}$ . Therefore, it is expected that this device would still have an apparent cutoff wavelength determined by  $\phi_{SiGe}$ , just as a device without this barrier layer would. The quantum yield will be reduced due to this barrier, however, especially when the photon energy lies between  $\phi_{Si}$  and  $\phi_{SiGe}$ . It is clear that the one parameter (the barrier height) Fowler theory can not be directly applied in this situation.

To model the effects of this thin tunneling barrier on the spectral response curve, and to provide a way to accurately extract barrier height from experimental data, we propose a simple model based on the following hypothesis which is very much in

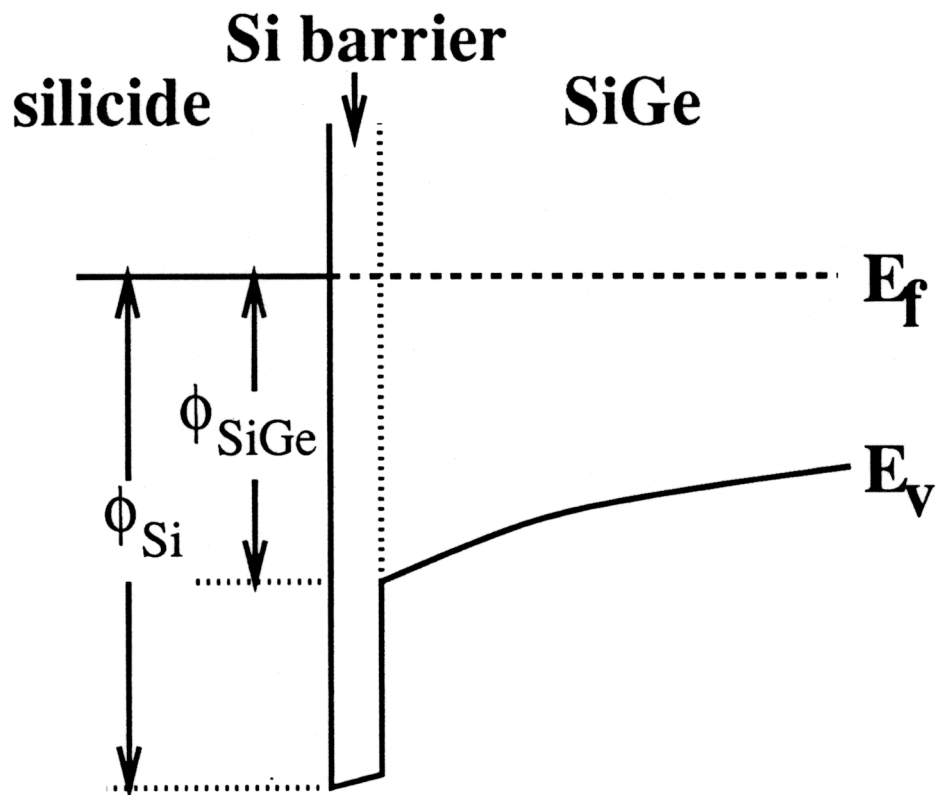


Figure 6.11: Schematic band diagram of a silicide/Si<sub>1-x</sub>Ge<sub>x</sub> detector with a parasitic silicon barrier.

parallel to that of Fowler's theory: the quantum yield is proportional to the integral of the hole-density-of-states in the metal weighted by holes' transmission coefficients through the silicon barrier into the Si<sub>1-x</sub>Ge<sub>x</sub> layer, where the transmission coefficients are to be evaluated after the hole energies normal to the surface are augmented by the photon energy  $h\nu$ .

One complication introduced in this model is the need to evaluate the transmission coefficient of a hole through the silicon barrier. A first principles calculation is extremely difficult because it would require not only detailed knowledge of the band structures of the metal, silicon, and strained Si<sub>1-x</sub>Ge<sub>x</sub> alloy, but also knowledge of all wave functions involved. Therefore, in our model an approximation for calculating the hole transmission coefficient was used primarily for its simplicity of implementation. The transmission coefficient of a hole into the semiconductor was assumed to be zero for energies below  $\phi_{SiGe}$ , a constant ( $T_0$ ) for energies above  $\phi_{Si}$ , and given by  $T = T_0 e^{-2\kappa w}$  for energies between  $\phi_{Si}$  and  $\phi_{SiGe}$ , where  $w$  is the Si barrier width, and  $\kappa$  is the imaginary part of the wave vector for a hole inside the barrier layer which was calculated using simple effective mass theory. Although simple, note that the model converges to Fowler's theory when the barrier width is zero (as in an ideal silicide/Si<sub>1-x</sub>Ge<sub>x</sub> detector) or infinite thick (as in a conventional silicide/Si device).

Based on the above hypothesis and assumption, the spectral response of a Schottky barrier detector with a thin tunneling barrier is derived as

$$\frac{Y}{T^2} \propto \left[ \int_0^\infty \ln \left( 1 + e^{-y + (h\nu - \phi_{Si})/kT} \right) dy + \int_0^{(\phi_{Si} - \phi_{SiGe})/kT} \ln \left( 1 + e^{-y + (h\nu - \phi_{SiGe})/kT} \right) e^{-A\sqrt{y}} dy \right] \quad (6.7)$$

where  $A = \sqrt{2m^*kT\omega^2/\hbar^2}$  ( $m^*$  is the hole effective mass in silicon). The first term corresponds to photoemission of holes over the silicon barrier into the Si<sub>1-x</sub>Ge<sub>x</sub> alloy, and it is identical to the results given by the Fowler theory for a barrier height of  $\phi_{Si}$ . The second term, which vanishes at infinite barrier width  $w$ , represents the contribution from holes tunneling through the silicon barrier. When the barrier width

$w$  is zero, these two terms can be combined leading to a Fowler expression for a barrier of height  $\phi_{\text{SiGe}}$ . The above equation was then numerically evaluated as a function of photon energy to obtain a spectral response.

As an example, we have calculated the spectral response of a hypothetical Pd<sub>2</sub>Si/Si<sub>1-x</sub>Ge<sub>x</sub> detector with a parasitic silicon barrier, and the results for several different barrier widths are shown in Fig. 6.12. When the barrier layer is absent ( $w=0$ ), the device is an ideal silicide/Si<sub>1-x</sub>Ge<sub>x</sub> Schottky barrier detector with a barrier height of 260meV. The Fowler plot is a straight line, as expected from Fowler's theory. As the barrier width increases, the curve bends downward between  $\phi_{\text{SiGe}}$  and  $\phi_{\text{Si}}$  dragging down the yield for photo energies above  $\phi_{\text{Si}}$  as well. When the barrier width increases to 10Å, a noticeable knee has developed around 420 meV. As the barrier width further increases to 50Å, it essentially becomes a conventional pure silicon device without any barrier height reduction.

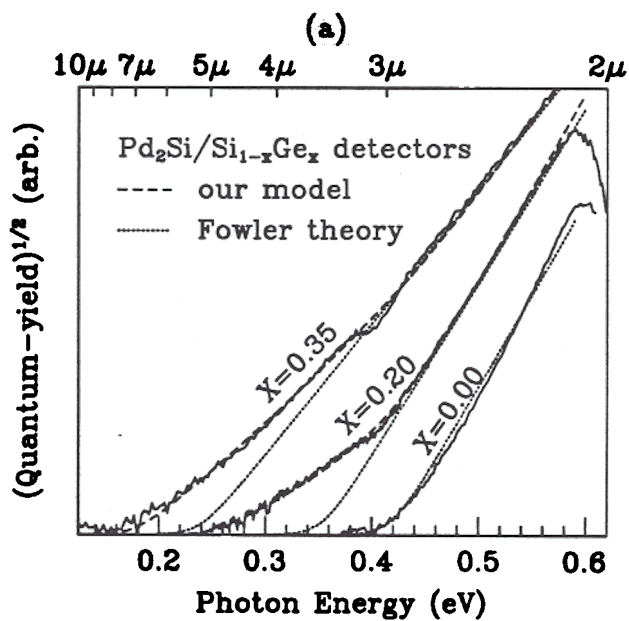
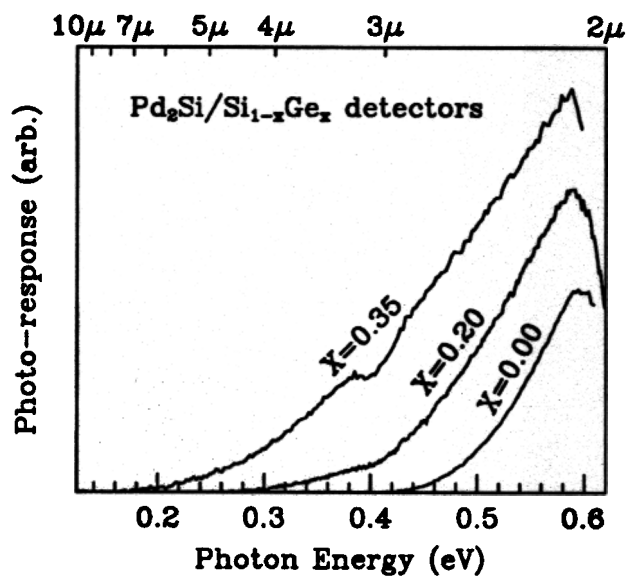
### 6.3 Pd<sub>2</sub>Si/Si<sub>1-x</sub>Ge<sub>x</sub> Schottky-Barrier IR Detectors

Palladium silicide (Pd<sub>2</sub>Si) has a Schottky-barrier height to p-type silicon of  $\sim 420\text{meV}$ , which corresponds to a cutoff wavelength of  $3\mu\text{m}$ . In the preceding section, it has been demonstrated that a silicon sacrificial layer can eliminate Ge segregation and Fermi level pinning, and Pd<sub>2</sub>Si/Si<sub>1-x</sub>Ge<sub>x</sub> has a lower barrier than Pd<sub>2</sub>Si/Si. In this section, attention will be paid to the dependence of Schottky-barrier height on the Ge concentration and the reverse leakage characteristics of Pd<sub>2</sub>Si/Si<sub>1-x</sub>Ge<sub>x</sub> detectors.

#### 6.3.1 Schottky-Barrier Height and Cut-off Wavelength

To examine how the Schottky-barrier height changes with Ge fraction, three different Pd<sub>2</sub>Si/Si<sub>1-x</sub>Ge<sub>x</sub> devices were fabricated, and the Ge concentrations ( $x$ ) in the films were 0,  $0.20 \pm 0.02$ , and  $0.35 \pm 0.02$  respectively. The silicon sacrificial layer thickness

was 100Å, and the deposited Pd layer was 150Å. The process sequence was the same as described before (Figure 6.9). The photo-response of the devices at zero bias were measured at 77K using a FT-IR spectrometer, and they are plotted in Figure 6.13(a). (The dips in the spectra at  $\sim 0.4\text{eV}$  are due to the absorption in the beam-splitter in the measurement instrument.) As the Ge fraction in the film is increased, the cut-off of the device was pushed to longer wavelength, indicating a lower barrier height, as expected. To accurately obtain the barrier heights, we first fit the spectral response of the Pd<sub>2</sub>Si/Si device with the Fowler theory, and a barrier height of 420meV was found. For the Pd<sub>2</sub>Si/Si<sub>0.80</sub>Ge<sub>0.20</sub> and Pd<sub>2</sub>Si/Si<sub>0.65</sub>Ge<sub>0.35</sub> devices, the kink near 420meV in their response curves (Fig. 6.13(b)) suggested that a thin layer of excess sacrificial silicon was left in these devices. Therefore, we fit the response curves of the Pd<sub>2</sub>Si/Si<sub>0.80</sub>Ge<sub>0.20</sub> and Pd<sub>2</sub>Si/Si<sub>0.65</sub>Ge<sub>0.35</sub> devices with the modified Fowler theory described earlier, using  $\phi_{Si} = 420\text{meV}$  and leaving  $\phi_{SiGe}$  and interfacial barrier width  $w$  as two adjustable parameters. Our modified Fowler theory gave much better fit to the experimental data than does Fowler theory (Figure 6.13(b)). From best fit we found Schottky-barrier heights of 260 and 170 meV, and interfacial silicon barrier widths of 10 and 3Å for Pd<sub>2</sub>Si/Si<sub>0.80</sub>Ge<sub>0.20</sub> and Pd<sub>2</sub>Si/Si<sub>0.65</sub>Ge<sub>0.35</sub>, respectively. The thicknesses of the excess silicon layers found from best fit were consistent with the process control we had in our laboratories. The results of barrier heights from photoresponse measurement are summarized in the Figure 6.14 which shows the Schottky-barrier height of Pd<sub>2</sub>Si/Si<sub>1-x</sub>Ge<sub>x</sub> obtained from photoresponse measurement as a function of Ge fraction  $x$ . The barrier height indeed decreases with increasing Ge fraction as expected. By extrapolating the data of Fig. 6.14, one sees that to achieve a cutoff wavelength of 10 $\mu\text{m}$ , a Ge fraction higher than 0.4 would be needed in the palladium silicide detectors.



(b)

Figure 6.13: Photoresponse of Pd<sub>2</sub>Si/Si<sub>1-x</sub>Ge<sub>x</sub> IR detectors by FT-IR. Note while our model gives excellent fit to experimental spectra, the Fowler theory gives very poor fit.

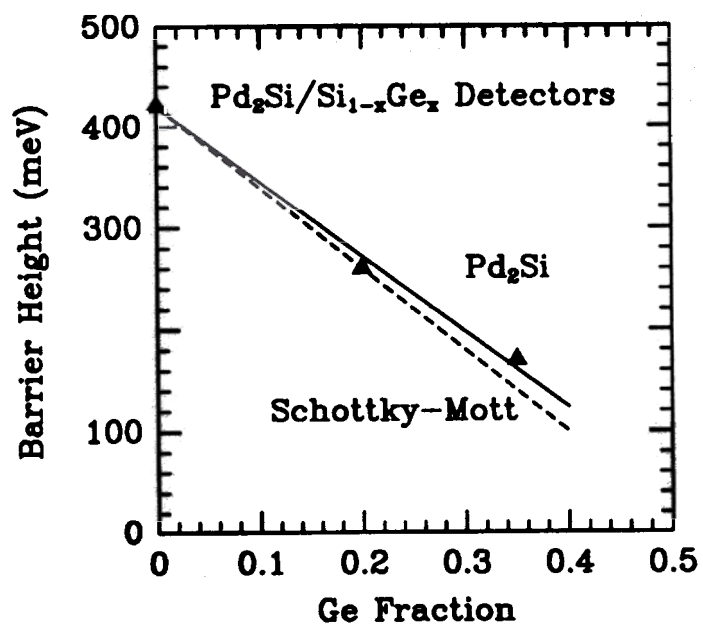


Figure 6.14: Schottky-barrier height of Pd<sub>2</sub>Si/Si<sub>1-x</sub>Ge<sub>x</sub> versus Ge fraction by photoresponse measurement

### 6.3.2 Reverse Leakage Current

For infrared focal plane array applications, low reverse leakage current of the detector element is required for high sensitivity. In this section, temperature dependent leakage current of the Pd<sub>2</sub>Si/Si<sub>1-x</sub>Ge<sub>x</sub> detectors is characterized. It is shown that ideally low leakage levels can be obtained from these devices.

#### Thermionic emission theory

For the p-type metal-semiconductor Schottky-contact, the reverse leakage current includes several different mechanisms, such as thermionic emission of holes from metal into semiconductor, minority carrier (electron) diffusion, and electron-hole generation within the space charge region. From thermionic emission theory, which assumes that thermionic hole emission is the dominant current transport mechanism, the I-V characteristic is given by

$$J = A^*T^2 e^{-q\phi_B/kT} \left( e^{qV/kT} - 1 \right) \quad (6.8)$$

where  $J$  is the current density,  $A^*$  the effective Richardson constant,  $\phi_B$  the Schottky-barrier height, and  $V$  the applied bias,  $k$  the Boltzmann constant,  $q$  the electron charge, and  $T$  the absolute temperature. From temperature dependent leakage current measurement, accurate Schottky-barrier height can be obtained by fitting the above equation provided that the thermionic emission model is valid, i.e. the dominant current component is from thermionic hole emission.

According to thermionic emission theory, the reverse leakage current does not explicitly depend on the applied reverse bias. The bias, however, can affect the leakage current through image-force induced barrier height lowering, which can be substantial especially at high doping levels and high biases. Thus, it is important to keep the doping level at a minimum to avoid excess reverse leakage at high biases.

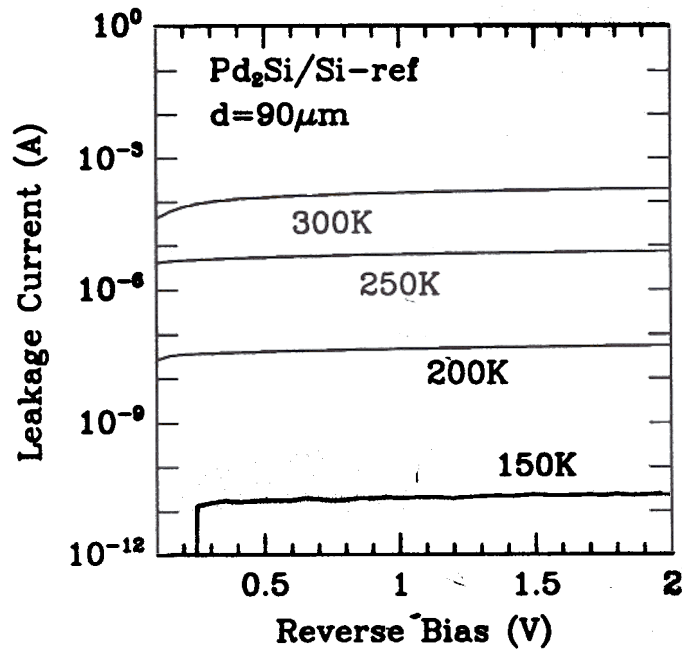


Figure 6.15: Reverse leakage characteristics of a Pd<sub>2</sub>Si/Si diode.

### Experimental results

Current-voltage characteristics of all devices were measured in a low temperature station from 90 to 300 Kelvin. For convenience, most measurements were done in a back-to-back configuration with the forward biased devices at least 20 times larger than the reverse biased one, which permits accurate measurement of the reverse bias I-V characteristics of the smaller device. Very little device-to-device variation was observed across the samples, indicating high uniformity.

Shown in Figure 6.15 is the leakage current of an all-silicon device ( made by direct silicidation of 10-20Ωcm silicon substrate ) as a function of applied reverse bias at various temperatures. The device has a circular geometry with a diameter of 90μm. We see very little dependence of leakage current on reverse bias, and the

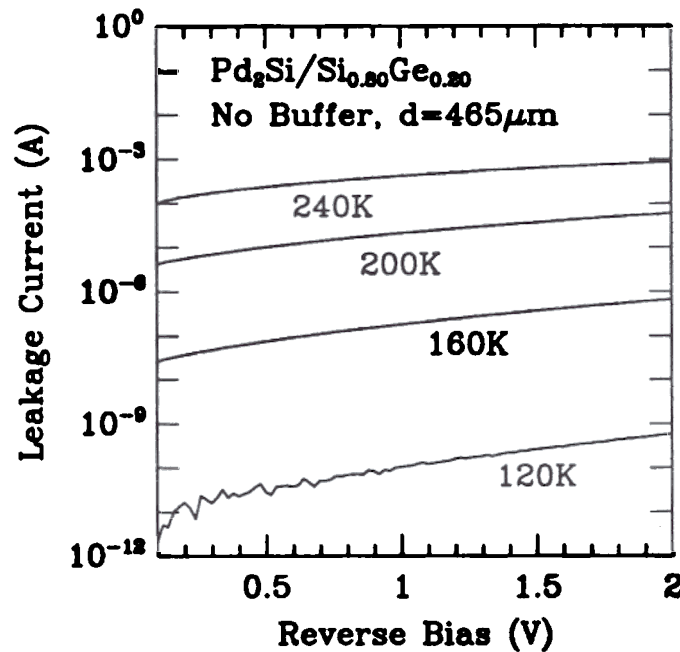


Figure 6.16: Reverse Leakage characteristics of sample #1058.

leakage level drops rapidly with decreasing temperature, indicating thermionic hole emission. To further confirm this, we plot the leakage current density over temperature square ( $J/T^2$ ) at 2V reverse bias versus inverse temperature in an Arrhenius plot (Figure 6.17). The data points can be well fit by a straight line, and from its slope a Schottky-barrier height of 379meV was obtained, which is consistent with the Schottky-barrier height found by photoresponse measurement (420meV).

Sample #1058, which has a Ge fraction of 0.20, had a higher leakage current than the all-silicon device at the same temperatures (Figure 6.16) because of the lower Schottky-barrier height. From fitting of the temperature dependent leakage current to the thermionic emission theory (Figure 6.17), a Schottky-barrier height of 269meV was found. It agrees well with the barrier height of 260meV found by photoresponse measurement, indicating ideally low leakage levels.

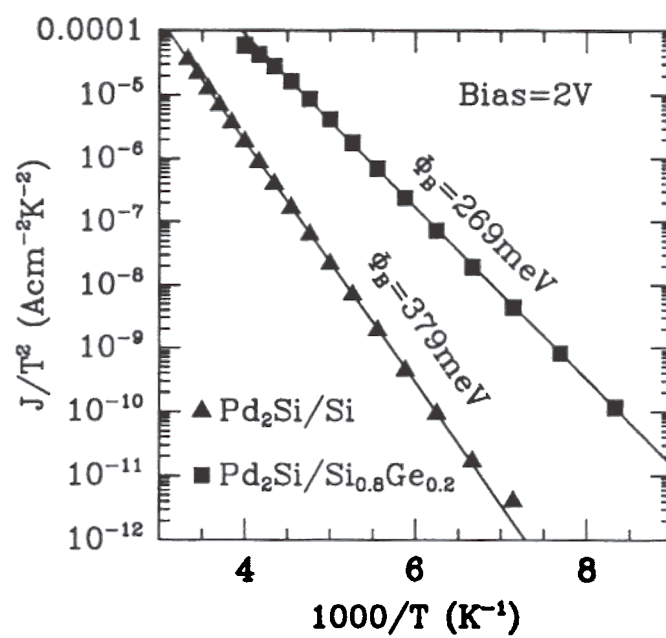


Figure 6.17: Temperature dependent leakage current of Pd<sub>2</sub>Si/Si<sub>1-x</sub>Ge<sub>x</sub> detectors at 2V reverse bias .

The  $\text{Pd}_2\text{Si}/\text{Si}_{0.65}\text{Ge}_{0.35}$  device, which had a barrier height of 170meV by photore-sponse measurement, showed an excess reverse leakage above that expected from ideal thermionic emission theory. The cause of this excess leakage is not known, however.

## 6.4 $\text{PtSi}/\text{Si}_{1-x}\text{Ge}_x$ Schottky-Barrier IR Detectors

Since palladium silicide has a relatively high barrier height (420meV) to silicon, in order to achieve operation beyond  $10\mu\text{m}$ , a Ge fraction more than 40% is required for  $\text{Pd}_2\text{Si}/\text{Si}_{1-x}\text{Ge}_x$  detectors. The critical thickness for  $x=0.40$  is less than  $40\text{\AA}$ , which renders fabrication of such devices difficult if not impossible. Platinum-silicide has a Schottky-barrier height of about 250meV to p-type silicon, which is more than 100 meV lower than that of palladium-silicide. By introducing only 20% Ge the cutoff wavelength of the standard PtSi/Si array technology could be extended from  $5\mu\text{m}$  to beyond  $10\mu\text{m}$ . Therefore, these structures were investigated.

### 6.4.1 Device Processing

Two platinum-silicide devices were studied. One was a conventional PtSi/Si Schottky-barrier diode directly fabricated on a p-type silicon substrate. The other was a  $\text{PtSi}/\text{Si}_{0.85}\text{Ge}_{0.15}$  device. The graded layer thickness was about  $200\text{\AA}$ , and the constant Ge layer thickness was about  $400\text{\AA}$ . The silicon sacrificial layer was  $\sim 40\text{\AA}$ . The device process sequence was the same as the palladium-silicide devices except for the metal deposition and anneal step. A  $25\text{\AA}$  layer of Pt was deposited at the SRI David Sarnoff Research Center.

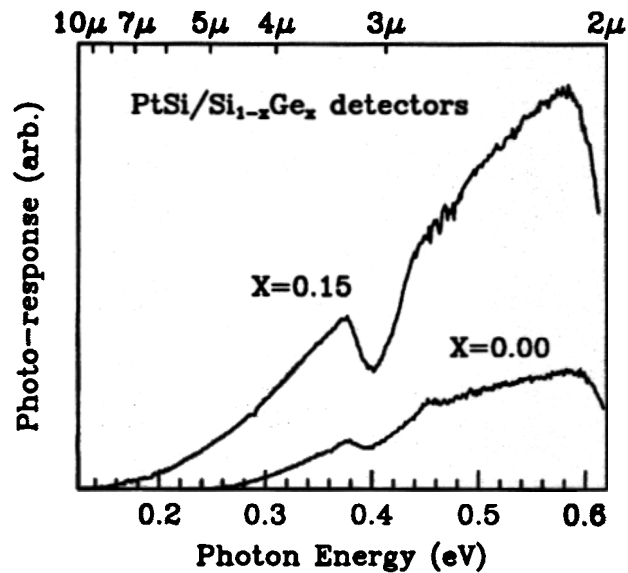
### 6.4.2 Cut-off Wavelength and Barrier Height

The spectral response of the devices operating in a short-circuit current mode was characterized at 77K using the Bomem FT-IR spectrometer. Intentionally scratched large-area devices were used in conjunction with the backside aluminum as the substrate contact to ensure a low series resistance. The measured results are shown in Figure 6.18, in which the quantum efficiency (in arbitrary units) was plotted vs photon energy for both the PtSi/Si control and the PtSi/ $\text{Si}_{0.85}\text{Ge}_{0.15}$  devices. From best fits obtained using the Fowler theory (for the PtSi/Si detector) and the modified Fowler theory (for the PtSi/ $\text{Si}_{0.85}\text{Ge}_{0.15}$  detector) (Figure 6.18(b)), Schottky-barrier heights of 240meV and 140meV were found for the PtSi/Si and PtSi/ $\text{Si}_{0.85}\text{Ge}_{0.15}$  detectors, respectively, corresponding to a barrier height reduction of 100 meV. The cutoff wavelength of the PtSi/ $\text{Si}_{0.85}\text{Ge}_{0.15}$  detector was extended to  $8.8\mu\text{m}$  from the  $5.2\mu\text{m}$  of the PtSi/Si detector.

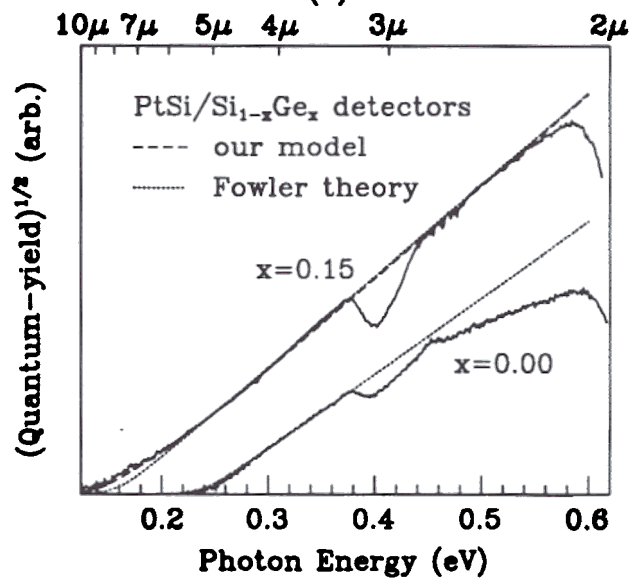
The Schottky-barrier heights of PtSi/ $\text{Si}_{1-x}\text{Ge}_x$  and Pd<sub>2</sub>Si/ $\text{Si}_{1-x}\text{Ge}_x$  detectors measured by spectral response are shown in Figure 6.19 as functions of Ge fraction. For both the palladium and platinum silicide devices, the Schottky-barrier height decreases with increasing Ge fraction as expected. From extrapolation, it is expected that the  $10\mu\text{m}$  cut-off wavelength can be achieved in a PtSi/ $\text{Si}_{1-x}\text{Ge}_x$  detector with as little as 20% Ge in the alloy.

### 6.4.3 Leakage Current

In contrast to the simple palladium devices, which had ideally low leakage levels, the first batch of platinum silicide devices with similar structures (no guard ring) were very leaky. The temperature dependent dark current at 2V reverse bias of an all-silicon control device was shown in Figure 6.20. At low temperatures, an excess leakage is evident. From the best fit to the thermionic emission theory, we



(a)



(b)

Figure 6.18: Experimental spectral responses of the platinum silicide detectors (solid lines), and best fits obtained using the Fowler theory (dotted lines) and our modified Fowler theory (dashed lines). (Dip at 0.4eV is artifact of the measurement instrument.)

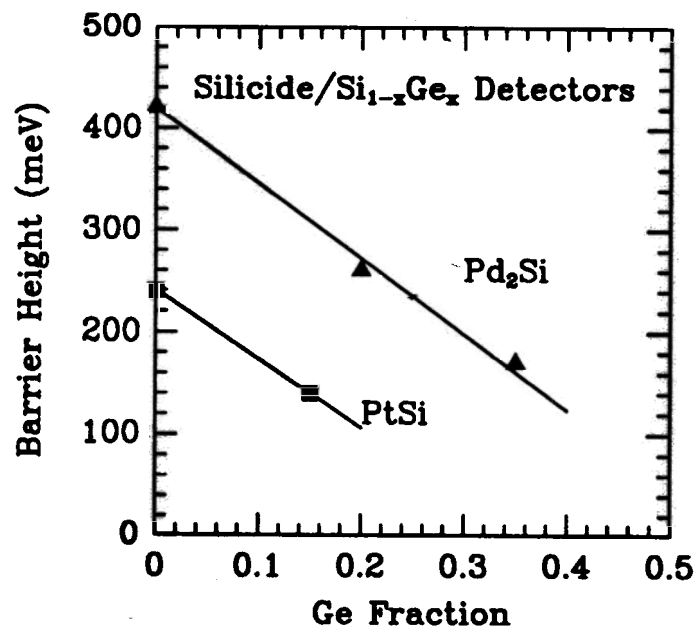


Figure 6.19: Pd<sub>2</sub>Si/Si<sub>1-x</sub>Ge<sub>x</sub> and PtSi/Si<sub>1-x</sub>Ge<sub>x</sub> Schottky-barrier heights versus Ge fraction (with sacrificial layer).

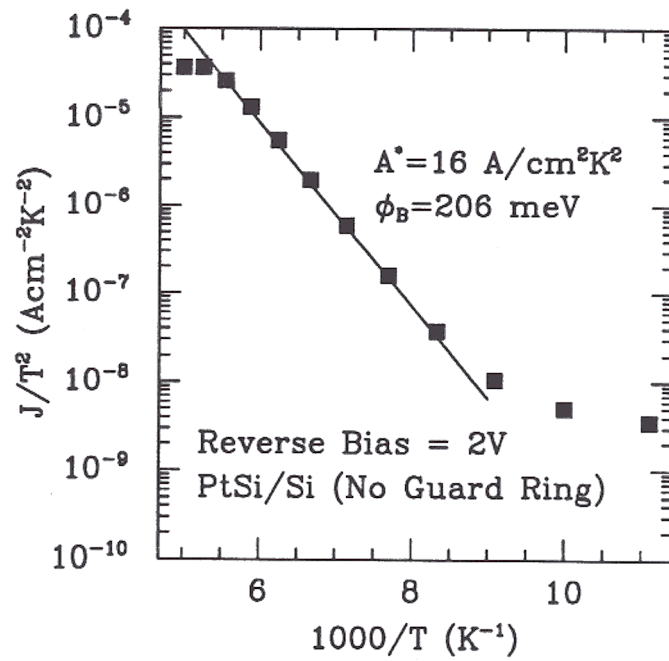
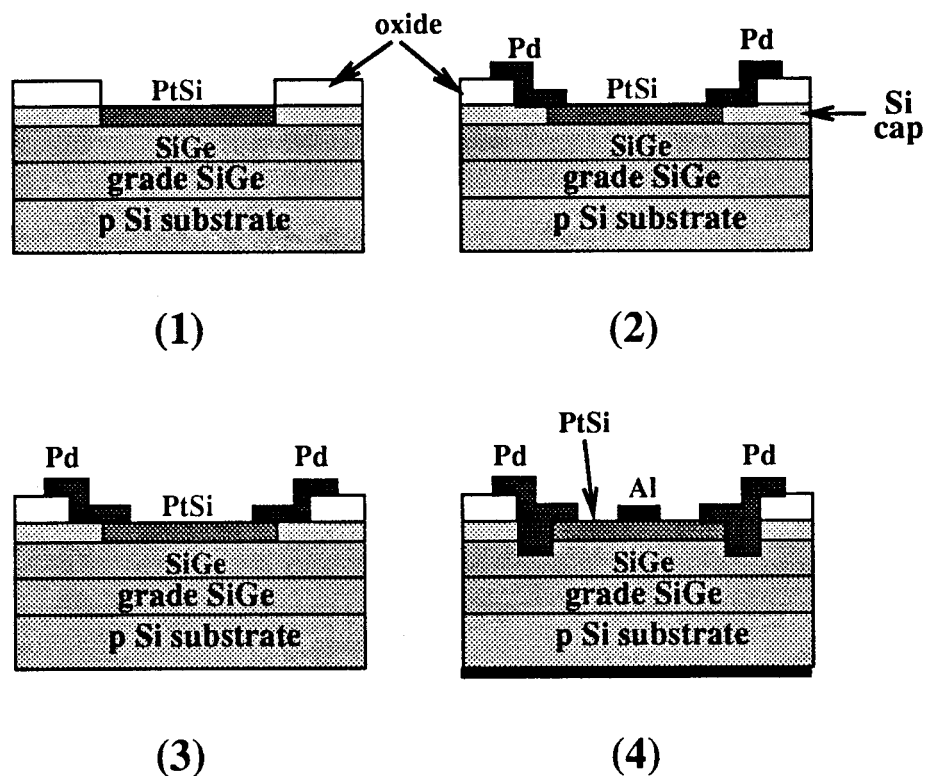


Figure 6.20: Reverse leakage characteristics of a PtSi/Si diode without a guard ring.

obtained a barrier height 206 meV, which was 34 meV below the value measured by spectral response, and an effective Richardson constant of 0.1A/cm<sup>2</sup>K<sup>2</sup>, orders of magnitude below the 10 – 100A/cm<sup>2</sup>K<sup>2</sup> normal range. All of these indicate edge leakage, possibly due to sharp curvature effects.

A common solution to the edge leakage problem is using a guard ring which creates a wider depletion layer thickness around the periphery of the device. Since the palladium silicide has a higher barrier height to silicon than the platinum silicide, it can be used for the guard ring purpose. The additional processing steps for creating the Pd<sub>2</sub>Si guard ring are shown schematically in Figure 6.21. After the PtSi step, the oxide layer was etched back leaving a ring of exposed silicon around the edge of PtSi. Then, a layer of Pd was deposited on top by lift-off, and heat treated to form a Pd<sub>2</sub>Si guard ring self-aligned to the PtSi. Finally, aluminum pads were deposited for contact.

Shown in Figure 6.22 are the temperature dependent leakage characteristics of the PtSi/Si<sub>1-x</sub>Ge<sub>x</sub> devices with a Pd<sub>2</sub>Si guard ring. For comparison, the data of the previous PtSi/Si device which did not have a guard ring are also shown in the figure. With the palladium silicide guard ring, much lower reverse leakage levels were observed. From a best fit to the thermionic emission theory, a barrier height of 236 meV was found for the PtSi/Si junction, which agrees well with the value of 240 meV from infrared spectral response, indicating ideally low leakage levels. The extracted effective Richardson constant was 12A/cm<sup>2</sup>K<sup>2</sup>, within the normal range. For the PtSi/Si<sub>0.85</sub>Ge<sub>0.15</sub> device with a guard ring, the barrier height from the leakage measurement was 103 meV, 37meV less than optical value of 140meV. The sources of this difference were not very clear, it may due to defects introduced during device processing. It is believed, however, that by employing a diffused guard ring and a more elaborate process, ideally low leakage levels can be obtained from PtSi/Si<sub>1-x</sub>Ge<sub>x</sub> devices.



1. starting structure (PtSi in windows)
2. oxide etch back and Pd deposition
3. formation of palladium-silicide by anneal
4. aluminum contact metalization

Figure 6.21: Fabrication of Pd<sub>2</sub>Si guard ring.

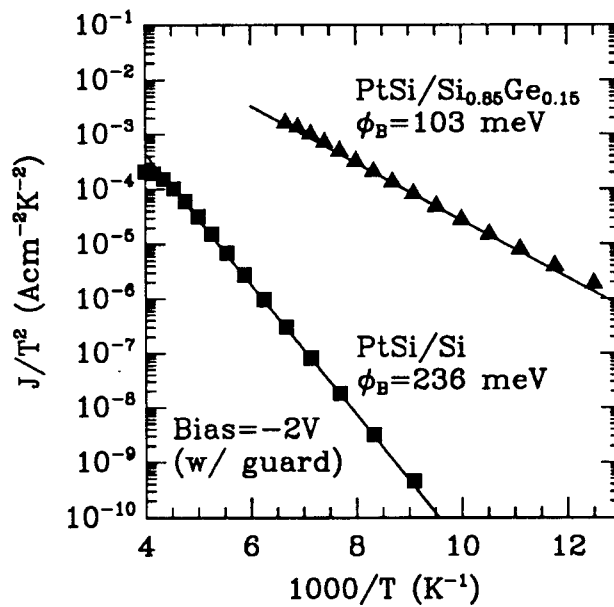
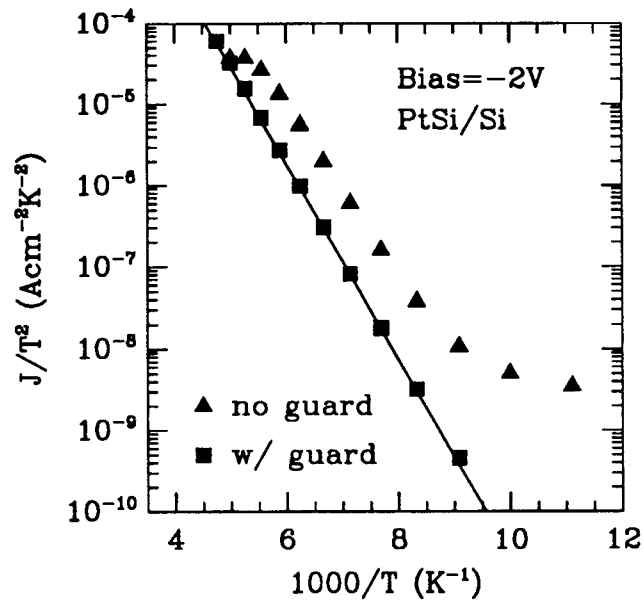


Figure 6.22: Reverse leakage characteristics of PtSi/Si and PtSi/Si<sub>1-x</sub>Ge<sub>x</sub> diodes with and without Pd<sub>2</sub>Si guard rings.

#### 6.4.4 External Quantum Efficiency

External quantum efficiency, which is defined as the number of current-contributing carriers generated per incident photon, is a very important figure-of-merit for an infrared detector. For high detectivity, it is desirable to have the highest quantum efficiency possible.

In the discussion in Section 6.1.2 it was shown that the external quantum efficiency of a Schottky-barrier detector can be approximated by

$$Y = C_1(h\nu - \phi_B)^2 \quad (6.9)$$

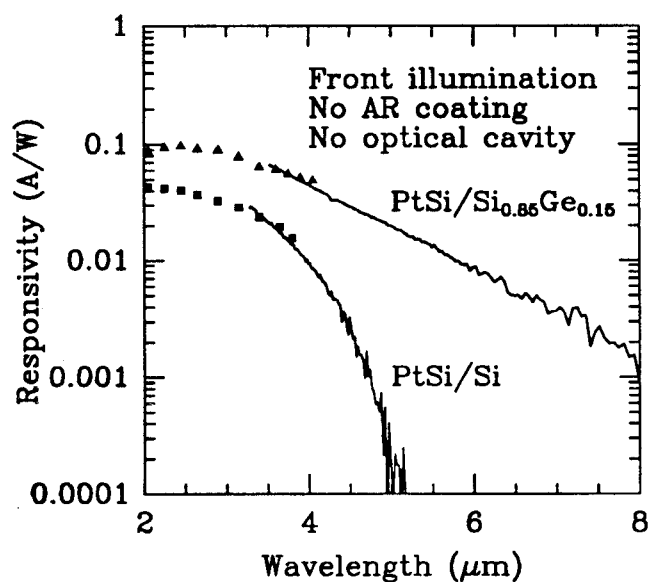
where  $C_1$  is the quantum efficiency coefficient, and  $\phi_B$  is the Schottky barrier height. It has been shown that by using Si<sub>1-x</sub>Ge<sub>x</sub>, a lower barrier height  $\phi_B$  was obtained in the PtSi/Si<sub>1-x</sub>Ge<sub>x</sub> detector compared to that of PtSi/Si. The quantum efficiency coefficient, however, is more of a property of the metal electrode (PtSi in this case) than that of the semiconductor. It is primarily determined by the optical absorption and hot hole relaxation processes in the metal. Therefore, a comparable value  $C_1$  was expected from the PtSi/Si detectors and the PtSi/Si<sub>1-x</sub>Ge<sub>x</sub> detectors, which meant a higher quantum efficiency for the PtSi/Si<sub>1-x</sub>Ge<sub>x</sub> detectors as well as a longer cutoff wavelength.

To find the external quantum efficiency as a function of wavelength, an infrared monochromator was used as the light source, and a pyroelectric detector with a known responsivity was used for calibration. The short circuit photocurrent of the detector was measured using standard lock-in techniques. Since this was not an optimized device in many ways, care was taken to ensure that the results would not be affected by device parasitics. The detector can be modeled as a current source with a shunt resistance due to leakage and a series resistance mainly due to the contact and substrate resistance. In order to correctly measure the photocurrent, the shunt resistance must be much larger than the sum of the series resistance and the input impedance of

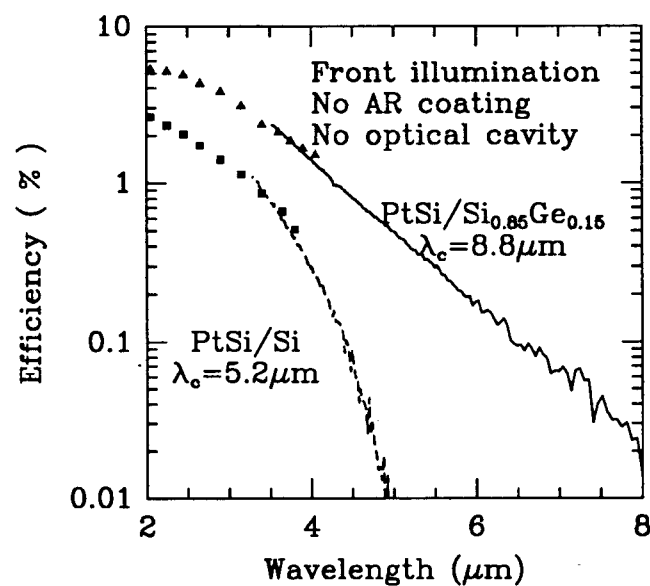
the current amplifier. To minimize the contact resistance, a large-area intentionally-scratched PtSi electrode was connected to the aluminum evaporated onto the backside of the sample, and it served as the substrate contact. Note that the backside was not intentionally doped and actually had a Si<sub>1-x</sub>Ge<sub>x</sub> layer too. The device was mounted on the cold head of a Helitran and cooled down to 40K. Measured quantum efficiencies decreased at both higher and lower temperatures presumably due to lower shunt resistance and higher substrate resistance, respectively. External quantum efficiencies of both the PtSi/Si control device and the PtSi/Si<sub>1-x</sub>Ge<sub>x</sub> detector were measured, and the results are shown in Figure 6.23 (filled triangles and squares). Because the limitation of the monochromator used, accurate measure of responsivity beyond 4 $\mu$ m could not be obtained, and the results of spectral response measured by FT-IR at 77K (which is a much more sensitive technique) were scaled to match the quantum efficiencies at 4 $\mu$ m. The measured external quantum efficiency of the PtSi/Si<sub>0.85</sub>Ge<sub>0.15</sub> detector was 0.10 A/W at 2.5 $\mu$ m, which is more than two times higher than that of the conventional PtSi/Si detector. The PtSi/Si<sub>0.85</sub>Ge<sub>0.15</sub> detector offers superior responsivity to the PtSi/Si detector over the whole wavelength range. From the best fit to the Fowler model, we found quantum efficiency coefficients of 0.25 and 0.26 for the PtSi/Si<sub>0.85</sub>Ge<sub>0.15</sub> and PtSi/Si detectors(Fig. 6.18(b)), respectively, which was consistent with the fact that both devices had the same silicide electrode and should give similar quantum efficiency coefficients. We conclude that the enhanced responsivity of the PtSi/Si<sub>1-x</sub>Ge<sub>x</sub> detector was due to its lower Schottky-barrier height.

## 6.5 Conclusion

In this Chapter, it has been demonstrated that silicide/Si<sub>1-x</sub>Ge<sub>x</sub> infrared detectors have longer cutoff wavelengths than their pure silicon counterparts. Cutoff wavelengths of 6.6 $\mu$ m and 8.8 $\mu$ m have been achieved in Pd<sub>2</sub>Si/Si<sub>0.65</sub>Ge<sub>0.35</sub> and PtSi/Si<sub>0.85</sub>Ge<sub>0.15</sub>



(a)



(b)

Figure 6.23: Responsivity and external quantum efficiency of PtSi/Si<sub>1-x</sub>Ge<sub>x</sub> Schottky-barrier IR detectors.

detectors, respectively, and a cutoff beyond  $10\mu\text{m}$  is expected in a  $\text{PtSi}/\text{Si}_{0.80}\text{Ge}_{0.20}$  detector.

It has been experimentally shown that a silicon sacrificial layer is necessary to obtain the desired barrier height reduction in the silicide/ $\text{Si}_{1-x}\text{Ge}_x$  Schottky contacts. The silicon sacrificial layer ensures the formation of a pure silicide on the  $\text{Si}_{1-x}\text{Ge}_x$  alloy, and at the same time eliminates the Ge segregation at the interface which could cause Fermi level pinning and an increased Schottky barrier height.

In our experiments, higher quantum efficiencies were obtained from the  $\text{PtSi}/\text{Si}_{1-x}\text{Ge}_x$  detectors than the conventional  $\text{PtSi}/\text{Si}$  Schottky-barrier infrared detector, which is attributed to the lower barrier height in the  $\text{PtSi}/\text{Si}_{1-x}\text{Ge}_x$  devices.

A modified Fowler theory has been proposed to model the effects on the spectral response curves of silicide/ $\text{Si}_{1-x}\text{Ge}_x$  detectors of a parasitic barrier due to an unreacted Si sacrificial layer, and good agreement with experimental data has been achieved.

The  $\text{PtSi}/\text{Si}_{1-x}\text{Ge}_x$  detector is a very promising candidate for long wavelength infrared imaging applications not only because of its high performance, but also because it requires only one additional process to incorporate the  $\text{PtSi}/\text{Si}_{1-x}\text{Ge}_x$  detectors into the standard  $\text{PtSi}$  Schottky-barrier focal plane array technology.

# Conclusion and Future Work

### 7.0.1 Progress Made with this Thesis

An all-silicon vertical-cavity Fabry-Perot optical intensity modulator at  $1.3\mu\text{m}$  has been developed.

Through a comparative study of photoluminescence from strained Si/Si<sub>1-x</sub>Ge<sub>x</sub> single wells and stepped wells, direct evidence of type-I band alignment for strained Si<sub>1-x</sub>Ge<sub>x</sub>/Si heterojunction has been obtained. The complete band line-up has been determined by a combination of band edge photoluminescence and heterojunction internal photoemission.

It has been experimentally demonstrated that at high temperature (77K) the photoluminescence from strained Si/Si<sub>1-x</sub>Ge<sub>x</sub>/Si quantum wells is due to electron-hole plasmas rather than due to excitons, except at very low excitation levels. The photoluminescence line-shape can be well fit by a convolution of occupied electron and hole densities of states

An energy shift of photoluminescence from strained Si/Si<sub>1-x</sub>Ge<sub>x</sub>/Si quantum wells due to quantum confinement has been observed for the first time, and the amount of shift agrees well with the hole ground state energy calculated by solving the effective-mass equations based on an  $6 \times 6$  Luttinger-Kohn Hamiltonian which includes strain effects.

By using a silicon sacrificial layer for silicide formation, silicide/ $\text{Si}_{1-x}\text{Ge}_x$  long-wavelength infrared detectors have been demonstrated for the first time. Low reverse leakage and high quantum efficiency has been achieved in such detectors. The fabrication of these devices requires only very minor modifications from the standard PtSi Schottky-barrier focal-plane-array technology, making it a promising candidate for long-wavelength IR imaging applications

### 7.0.2 Directions for Future Research

While a modified Fowler theory has been proposed in this thesis to model the effects of a parasitic interfacial barrier due to unreacted Si sacrificial layer in silicide/ $\text{Si}_{1-x}\text{Ge}_x$  detectors, and good fit to experimental photoresponse curves has been obtained with the barrier width as a adjustable parameter, a systematic experimental study of such effects can help to further test the validity of this theory and, at the same time, to establish a tolerance requirement on the process technology for fabricating these devices.

The development of silicide/ $\text{Si}_{1-x}\text{Ge}_x$  detectors was intended for IR focal-plane-array imager applications. Therefore, the next natural step is to demonstrate 2-D arrays using the detectors developed in this thesis.

## Appendix A

### Growth Details of Sample #1058

All samples used in this thesis were grown with a Rapid Thermal Chemical Vapor Deposition (RT-CVD) system under the control of a personal computer, which handles gas flow rates, switching of gases, closed-loop wafer temperature control, and timing of layer growth, etc. The growth parameters of the epitaxial layers of a typical  $\text{Pd}_2\text{Si}/\text{Si}_{0.80}\text{Ge}_{0.20}$  infrared detector (#1058) are given in Tabel A.1, and the "Sequencer Tables" used for its growth are also listed below.

Sample # 1058				
Time (sec)	Temp. ( $^{\circ}\text{C}$ )	Ge conc. (%)	$\text{GeH}_4$ flow (sccm)	Thickness ( $\text{\AA}$ )
80	700	0	0	40
302	625	0 $\rightarrow$ 20	0 $\rightarrow$ 100	150
240	625	20	100	400
200	700	0	0	100

Table A.1: Growth parameters for sample #1058

## Sequencer Table # 0

<u>Step</u>	<u>Action</u>	<u>Comment</u>
0	CONTROL ON&	turn on Control
1	SCAN ON(0,3)	and Scan simultaneously
2	SET(SP7,0)&	lamp power zero
3	SET(SP4,0)	turn off PID control
4	SET(SP0,0)	zero loop counter
5	SET(SP1,1)	not a superlattice
6	SET(DO0,1)	N <sub>2</sub> off
7	SET(DO2,0)&	
8	SET(DO3,1)&	select GeH <sub>4</sub>
9	SET(DO4,0)&	
10	SET(DO5,0)&	
11	SET(DO6,0)&	
12	SET(DO7,1)&	select DCS
13	SET(DO8,0)&	
14	SET(DO9,0)&	injects off
15	SET(DO10,0)&	
16	SET(DO11,0)&	
17	SET(DO12,0)&	
18	SET(DO13,0)	
19	SET(AO1,0.01)	flow rates down
20	SET(AO2,0.213)	GeH <sub>4</sub> flow 100 sccm
21	SET(AO3,0.01)	
22	SET(AO4,0.01)	
23	SET(AO5,0.01)	
24	SET(AO6,0.538)	DCS flow 26 sccm

25	SET(AO7,0.01)	
26	SET(DO15,1)	vaccum on
27	SET(DO1,1)	H <sub>2</sub> on
28	SET(AO2,0.62)	H <sub>2</sub> flow 3 slpm
29	WAITUNTIL(AI24>0.5)	press GO to start
30	SET(SP3,1)	read cold value
31	SEQUENCER ON(0.3,1,0)	start SEQUENCER # 1

## Sequencer Table # 1

<u>Step</u>	<u>Action</u>	<u>Comment</u>
0	SET(AO11,0)	pressure gauge : 1-1000 torr
1	SET(AO8, 0.25)	set pressure to 250 torr
2	SET(AO2, 0.8)	H <sub>2</sub> flow 4 slpm
3	SET(SP3, 0)	latch cold transmission
4	WAITUNTIL(AI29>0.24)	
5	WAIT(10)	
6	WAITUNTIL(AI29<0.26)	wait for stable pressure
7	RAMP(SP7, 0.4, 0.274)	ramp up T to 1000°C
8	WAIT(120)	2 minutes bake-out
9	SET(AO2, 0.62)	H <sub>2</sub> flow 3 slpm
10	SET(AO8, 0.0)	reduce pressure
11	WAITUNTIL(AI29 < 0.01)	wait until pressure < 10 torr
12	SET(AO11, 1)	switch to 10 torr gauge
13	WAITUNTIL(AI24 > 0.5)	
14	SET(SP2, 0)	
15	SEQUENCER ON(0.3, 7, 0)	call Sequencer # 7

16	WAITUNTIL(SP2 > 0.5)	wait until Seq 7 is done
17	SET(SP2, 0)	
18	SEQUENCER ON(0.3, 6, 0)	call Sequencer # 6
19	WAITUNTIL(SP2 > 0.5)	wait until Seq 6 is done
20	SET(SP2, 0)	
21	SEQUENCER ON(0.3, 5, 0)	call Sequencer # 5
22	WAITUNTIL(SP2 > 0.5)	wait until Seq 5 is done
23	SEQUENCER OFF (1)	end of growth

## Sequencer Table # 5

<u>Step</u>	<u>Action</u>	<u>Comment</u>
0	SET(DO3, 0)&	GeH <sub>4</sub> select off
1	WAIT(200)	100Å Si cap layer
2	SET(DO13, 0)	DCS inject off
3	SET(DO7, 0)	DCS select off
4	WAIT(10)	
5	SET(SP7, 0.10)&	lamp power 10%
6	SET(SP4, 0)	PID off
7	RAMP(SP7, -0.4, 0.0)	lamp off
8	SET(SP2, 1)	end of Seq 5

## Sequencer Table # 6

<u>Step</u>	<u>Action</u>	<u>Comment</u>
0	SET(SP5, 3.318)& SET(SP4, 1)&	set T to 700°C PID on

2	WAIT(60)	
3	SET(AO2, 0.0)&	GeH <sub>4</sub> flow 0 sccm
4	WAIT(10)	
5	SET(SP5, 2.440)&	set T to 625°C
6	WAIT(15)	
7	SET(DO10, 1)&	inject GeH <sub>4</sub>
8	RAMP(AO2, 0.07, 0.213)	graded Si <sub>1-y</sub> Ge <sub>y</sub>
9	WAIT(240)	400Å Si <sub>0.8</sub> Ge <sub>0.2</sub>
10	SET(DO10, 0)&	GeH <sub>4</sub> inject off
11	WAIT(15)	
12	SET(SP5, 3.318)&	T = 700°C
13	SET(AO2, 0.01)&	reduce GeH <sub>4</sub> flow
14	SET(SP2, 1)	end of Seq 6

## Sequencer Table # 7

<u>Step</u>	<u>Action</u>	<u>Comment</u>
0	SET(DO7, 1)	select DCS
1	SET(DO3, 1)	select GeH <sub>4</sub>
2	SET(AO6, 0.538)	DCS flow 26 sccm
3	SET(AO8, 0.6)	P=6 torr
4	WAITUNTIL(AI28 < 0.61)	
5	WAIT(5)	
6	WAITUNTIL(AI28 > 0.59)	
7	RAMP(SP7, -0.2, 0.160)	T down to 700°C
8	Wait(20)	
9	SET(DO13, 1)	inject DCS

10

SET(SP2, 1)

end of Seq 7

# Publications and Presentations Resulting from This Thesis

### Journal Articles

1. X. Xiao, J.C. Sturm, S.R. Parihar, S.A. Lyon, D. Meyerhofer, S. Palfrey, and F.V. Shallcross, "Silicide/strained  $\text{Si}_{1-x}\text{Ge}_x$  Schottky-barrier Infrared Detectors," *Elec. Dev. Lett.*, to be published.
2. X. Xiao, J.C. Sturm, S.R. Parihar, S.A. Lyon, D. Meyerhofer, S. Palfrey, and F.V. Shallcross, "Modelling of Parasitic Barrier Effects in Silicide/ $\text{Si}_{1-x}\text{Ge}_x$  Schottky-barrier Long Wavelength Infrared Detectors," *J. Vac. Sci. Tech.*, to be published.
3. Z. Matutinovic, C.W. Liu, X. Xiao, and J.C. Sturm, "Symmetric Si/ $\text{Si}_{1-x}\text{Ge}_x$  Electron Resonant Tunneling Diodes with an Anomalous Temperature Behaviour," *Appl. Phys. Lett.*, to be published.
4. J.C. Sturm, X. Xiao, P.V. Schwartz, C.W. Liu, L.C. Lenchyshyn, and M.L.W. The-walt, "Band-edge exciton luminescence from Si/strained  $\text{Si}_{1-x}\text{Ge}_x$ /Si structures", *J. Vac. Sci. and Tech. B*10(4), 1998(1992).

5. Q. Mi, X. Xiao, J.C. Sturm, L.C. Lenchyshyn, and M.L.W. Thewalt, "Room-temperature CW  $1.3\mu\text{m}$  Electroluminescence from Strained Si/Si<sub>1-x</sub>Ge<sub>x</sub> Quantum Wells," *Applied Physics Letters*, **60**, 3177(1992).
6. X. Xiao, C.W. Liu, J.C. Sturm, L.C. Lenchyshyn, and M.L.W. Thewalt, "Photoluminescence from Electron-Hole Plasmas Confined in Si/Si<sub>1-x</sub>Ge<sub>x</sub>/Si Quantum Wells," *Applied Physics Letters*, **60**, 1720(1992).
7. X. Xiao, C.W. Liu, J.C. Sturm, L.C. Lenchyshyn, and M.L.W. Thewalt, "Quantum Confinement Effects in Strained Silicon-Germanium Alloy Quantum Wells," *Applied Physics Letters*, **60**, 2135(1992).
8. X. Xiao, J.C. Sturm, K.K. Goel, and P.V. Schwartz, "Fabry-Perot Optical Intensity Modulator at  $1.3\mu\text{m}$  in Silicon," *IEEE Photonics Technology Letters* **3**, 230(1991).
9. E.J. Prinz, P.M. Garone, P.V. Schwartz, X. Xiao, and J.C. Sturm, "The Effect of Base Dopant Outdiffusion and Undoped Si<sub>1-x</sub>Ge<sub>x</sub> Junction Spacer Layers in Si/Si<sub>1-x</sub>Ge<sub>x</sub>/Si Heterojunction Bipolar Transistors," *IEEE Electron Device Letters*, **ED12-2**, 42(1991).

### Conference Papers

1. X. Xiao, J.C. Sturm, S.R. Parihar, S.A. Lyon, D. Meyerhofer, and S. Paley, "Silicide/Si<sub>1-x</sub>Ge<sub>x</sub> Schottky-barrier Long Wavelength Infrared Detectors," *IEEE IEDM Tech. Digest*, 125(1992).
2. E.J. Prinz, X. Xiao, P.V. Schwartz, and J.C. Sturm, "Increased Functionality of Si/SiGe/Si Heterojunction Bipolar Transistors," *AVS Topical Conference on Silicon Heterostructures*, Chicago, November 1992.

3. X. Xiao, J.C. Sturm, S.R. Parihar, S.A. Lyon, D. Meyerhofer, and S. Palfrey, "Silicide/Si<sub>1-x</sub>Ge<sub>x</sub> Schottky-barrier Long Wavelength Infrared Detectors," *AVS Topical Conference on Silicon Heterostructures*, Chicago, November 1992.
4. Z. Matutinovic, C.W. Liu, X. Xiao, and J.C. Sturm, "Electron Si/SiGe Resonant Tunneling Diode Grown by RTCVD," *AVS Topical Conference on Silicon Based Heterostructures*, Chicago, November 1992.
5. T.A. Kennedy, E.R. Glaser, D.J. Godbey, P.E. Thompson, C.H. Chern, K.L. Wang, X. Xiao, and J.C. Sturm, "ODMR of Sharp Luminescence from Si/Si<sub>1-x</sub>Ge<sub>x</sub> Superlattices," *AVS Topical Conference on Silicon Based Heterostructures*, Chicago, November 1992.
6. X. Xiao, J.C. Sturm, L.C. Lenchyshyn, and M.L.W. Thewalt, "Direct Evidence by Photoluminescence of Type-I Band Alignment for Strained Si<sub>1-x</sub>Ge<sub>x</sub> ( $x \leq 0.35$ ) on (100) Silicon," *Electronic Materials Conference*, Boston, June 1992.
7. E.J. Prinz, X. Xiao, P.V. Schwartz, and J.C. Sturm, "A Novel Double Base Heterojunction Bipolar Transistor for Low Temperature Bipolar Logic," *IEEE Device Research Conference*, Boston, June 1992.
8. Q. Mi, X. Xiao, J.C. Sturm, L.C. Lenchyshyn, and M.L.W. Thewalt, "Room-temperature CW 1.3 $\mu$ m and 1.5 $\mu$ m Electroluminescence from Si/Si<sub>1-x</sub>Ge<sub>x</sub> Quantum Wells," *IEEE Device Research Conference*, Boston, June 1992.
9. Q. Mi, X. Xiao, J.C. Sturm, L.C. Lenchyshyn, and M.L.W. Thewalt, "Room-temperature CW 1.3 $\mu$ m Electroluminescence from Si/Si<sub>1-x</sub>Ge<sub>x</sub> Quantum Wells," *IEEE Sarnoff Symp.* (1992).
10. X. Xiao, J.C. Sturm, L.C. Lenchyshyn, and M.L.W. Thewalt, "Photoluminescence Studies of Si/Si<sub>1-x</sub>Ge<sub>x</sub>/Si Single Quantum Wells and Hole Effective

- Masses," *IEEE Semiconductor Interface Specialists Conference*, Orlando, FL, Dec. 1991.
11. J.C. Sturm, X. Xiao, Q. Mi, and H. Manoharan, "Optical properties of  $\text{Si}_{1-x}\text{Ge}_x$  quantum wells and superlattices grown by rapid thermal chemical vapor deposition," *Proc. SPIE Symp.* 1595, 90(1991).
  12. X. Xiao, J.C. Sturm, K.K. Goel, and P.V. Schwartz, "Data Transmission at  $1.3\mu\text{m}$  using Silicon Spatial Light Modulator," *Proc. SPIE Symp.* 1476, 301(1991).
  13. J.C. Sturm, Q. Mi, X. Xiao, and P.V. Schwartz, "Well Resolved Band-edge Photo- and Electro-luminescence in Strained  $\text{Si}_{1-x}\text{Ge}_x$  Quantum Wells and Superlattices," *Proc. Int. Conf. on Solid State Devices and Materials*, in press(1991).
  14. J.C. Sturm, P.V. Schwartz, H. Manoharan, X. Xiao, and Q. Mi, "High Lifetime Strained  $\text{Si}_{1-x}\text{Ge}_x$  Films Grown by Rapid Thermal Chemical Vapor Deposition," *Proc. Symp. European Material Research Society*, (1991).
  15. J.C. Sturm, P. Prucnal, Y.M. Liu, H. Manoharan, Q. Mi, P.V. Schwartz, and X. Xiao, "Applications of  $\text{Si}_{1-x}\text{Ge}_x$  Strained Layer Alloys for Silicon-based Optical Interconnects," *Proc. IEEE Sarnoff Symp.* (1991).
  16. X. Xiao, J.C. Sturm, P.V. Schwartz, and K.K. Goel, "Vertical  $1.3\mu\text{m}$  Optical Modulator in Silicon-On-Insulator," *Proc. 1990 IEEE SOS/SOI Technology Conference*, 192(1990).
  17. E.J. Prinz, P.M. Garone, P.V. Schwartz, X. Xiao, and J.C. Sturm, "The Effect of Base-emitter Spacers and Strain-dependent densities of States in  $\text{Si}/\text{Si}_{1-x}\text{Ge}_x/\text{Si}$  Heterojunction Bipolar Transistors," *IEDM Technical Digest*, 639(1989).

18. J.C. Sturm, X. Xiao, P.M. Garone, and P.V.Schwartz, "Electron-Beam-Induced-Current (EBIC) Imaging of Defects in  $\text{Si}_{1-x}\text{Ge}_x$  Multilayer Structures," *Proc. Symp. Mat. Res. Soc.* **148**, 341(1989).

## References

- [1] J. P. Lorenzo and R. A. Soref, "1.3 $\mu\text{m}$  electro-optic silicon switch," *Appl. Phys. Lett.*, vol. 51, p. 6, 1987.
- [2] B. R. Hemenway, O. Solgaard, and D. M. Bloom, "All-silicon integrated optical modulator for 1.3 $\mu\text{m}$  fiber-optic interconnects," *Appl. Phys. Lett.*, vol. 55, no. 4, p. 349, 1989.
- [3] R. A. Soref and B. R. Bennet, "Electrooptical effects in silicon," *IEEE Journal of Quantum Electronics*, vol. QE-23, p. 123, 1987.
- [4] S. M. Sze, *Physics of Semiconductor Devices*. John Wiley & Sons, 2nd ed., 1981.
- [5] B. R. Hemenway, O. Solgaard, A. A. Godil, and D. M. Bloom, "A polarization-independent silicon light intensity modulator for 1.3 $\mu\text{m}$  fiber optics," *IEEE Photon. Tech. Lett.*, vol. 2, p. 262, 1990.
- [6] *Dr. R. Sundaesan of Texas Instruments supplied the SIMOX wafer used in this study.*
- [7] R. Hunsperger, ed., *Integrated Optics: Theory and Technology*, vol. Springer Series on Optical Science vol. 33. Springer-Verlag, 2nd ed., 1982.
- [8] J. H. van der Merwe, "Structure of epitaxial crystal interfaces," *Surface Sci.*, vol. 31, p. 198, 1972.

- [9] J. W. Mathews and A. E. Blakeslee, "Defects in epitaxial multilayers," *J. Crystal Growth*, vol. 27, p. 118, 1974.
- [10] R. People and J. C. Bean, "Calculation of critical layer thickness versus lattice mismatch for  $\text{Ge}_x\text{Si}_{1-x}/\text{Si}$  strained-layer heterostructures," *Appl. Phys. Lett.*, vol. 47, no. 3, p. 322, 1985.
- [11] R. Braunstein, A. R. Moore, and F. Herman, "Intrinsic optical absorption in germanium-silicon alloys," *Physical Review*, vol. 109, no. 3, p. 695, 1958.
- [12] R. People, "Indirect band gap of coherently strained  $\text{Ge}_x\text{Si}_{1-x}$  bulk alloys on  $\langle 001 \rangle$  silicon substrates," *Physical Review B*, vol. 32, no. 2, p. 1405, 1985.
- [13] J. C. Sturm, P. V. Schwartz, E. J. Prinz, and H. Manoharan, "Growth of  $\text{Si}_{1-x}\text{Ge}_x$  by rapid thermal chemical vapor deposition and application to heterojunction bipolar transistors," *J. Vac. Sci. Technol.*, vol. B9, p. 2011, 1991.
- [14] J. C. Sturm, P. M. Garone, and P. V. Schwartz, "Temperature control of silicon-germanium alloy epitaxy growth on silicon substrate by infrared transmission," *J. Appl. Phys.*, vol. 69, p. 542, 1991.
- [15] J. C. Sturm, P. M. Garone, E. J. Prinz, P. V. Schwartz, and V. Venkataraman, "Interface abruptness in epitaxial silicon and silicon-germanium structures grown by rapid thermal chemical vapor deposition," *Proc. Int. Conf. on CVD XI*, vol. 90-12, p. 295, 1990.
- [16] J. Weber and M. I. Alonso, "Near-band-edge photoluminescence of Si-Ge alloys," *Phys. Rev. B*, vol. 40, no. 8, p. 5683, 1989.
- [17] K. Terashima, M. Tajima, and T. Tatsumi, "Near-band-gap photoluminescence of  $\text{Si}_{1-x}\text{Ge}_x$  alloys grown on Si(100) by molecular beam epitaxy," *Appl. Phys. Lett.*, vol. 57, no. 18, p. 1925, 1990.

- [18] J. C. Sturm, H. Manoharan, L. C. Lenchyshyn, M. L. Thewalt, N. L. Rowell, J. P. Noel, and D. C. Houghton, "Well-resolved band-edge photoluminescence of excitons confined in strained  $\text{Si}_{1-x}\text{Ge}_x$  quantum wells," *Phys. Rev. Lett.*, vol. 66, no. 10, p. 1362, 1991.
- [19] J. P. Noel, N. L. Rowell, D. C. Houghton, and D. D. Perovic, "Intense photoluminescence between 1.3 and 1.8  $\mu\text{m}$  from strained  $\text{Si}_{1-x}\text{Ge}_x$  alloys," *Appl. Phys. Lett.*, vol. 57, no. 10, p. 1037, 1990.
- [20] R. Zachai, K. Eberl, G. Abstreiter, E. Kasper, and H. Kibbel, "Photoluminescence in short-period Si/Ge strained-layer superlattices," *Phys. Rev. Lett.*, vol. 64, p. 1055, 1990.
- [21] H. Okumura, K. Miki, S. Misawa, K. Sakamoto, T. Sakamoto, and S. Yoshida, "Observation of direct band gap properties in  $\text{Ge}_n\text{Si}_m$  strained-layer superlattices," *Japan. J. Appl. Phys.*, vol. 28, p. L1893, 1989.
- [22] U. Schmid, N. E. Christensen, and M. Cardona, "Direct transition energies in strained ten-monolayer Ge/Si superlattices," *Phys. Rev. Lett.*, vol. 65, p. 2610, 1990.
- [23] R. People, J. C. Bean, D. V. Lang, A. M. Sergent, H. L. Stormer, K. W. Wecht, R. T. Lynch, and K. Baldwin, "Modulation doping in  $\text{Ge}_x\text{Si}_{1-x}$ /Si strained layer heterostructures," *Appl. Phys. Lett.*, vol. 45, p. 1231, 1984.
- [24] R. People and J. C. Bean, "Band alignments of coherently strained  $\text{Ge}_x\text{Si}_{1-x}$ /Si heterostructures on  $\langle 001 \rangle \text{Ge}_y\text{Si}_{1-y}$  substrates," *Appl. Phys. Lett.*, vol. 48, no. 8, p. 538, 1986.
- [25] H. Jorke and H. J. Herzog, "Mobility enhancement in modulation-doped Si -  $\text{Si}_{1-x}\text{Ge}_x$  superlattice grown by molecular beam epitaxy," p. 352, 1985.

- [26] G. Abstreiter, H. Brugger, T. Wolf, H. Jorke, and H. J. Herzog, "Strain-induced two-dimensional electron gas in selectively doped Si/Si<sub>x</sub>Ge<sub>1-x</sub> superlattices," *Phys. Rev. Lett.*, vol. 54, no. 22, p. 2441, 1985.
- [27] C. G. V. de Walle and R. M. Martin, "Theoretical study of Si/Ge interfaces," *J. Vac. Sci. Technol.*, vol. B3, no. 4, p. 1256, 1985.
- [28] C. G. V. de Walle and R. M. Martin, "Theoretical calculations of heterojunction discontinuities in the Si/Ge system," *Phys. Rev. B*, vol. 34, p. 5621, 1986.
- [29] D. V. Lang, R. People., J. C. Bean, and A. M. Sergent, "Measurement of the band gap of Ge<sub>x</sub>Si<sub>1-x</sub>/Si strained-layer heterostructures," *Appl. Phys. Lett.*, vol. 47, no. 12, p. 1333, 1985.
- [30] S. Khorram, C. H. Chern, and K. L. Wang, "Measurement of valence band offset in strained Ge<sub>x</sub>Si<sub>1-x</sub>/Si heterojunctions," *Proc. Mat. Res. Soc. Symp.*, vol. 220, p. 181, 1991.
- [31] K. Nauka, T. I. Kamins, J. E. Turner, C. A. King, J. L. Hoyt, and J. F. Gibbons, "Admittance spectroscopy measurements of band offsets in Si/Si<sub>1-x</sub>Ge<sub>x</sub>/Si heterostructures," *Appl. Phys. Lett.*, vol. 60, no. 2, p. 195, 1992.
- [32] J. C. Sturm, E. J. Prinz, P. M. Garone, and P. V. Schwartz, "Band-gap shifts in silicon-germanium heterojunction bipolar transistors," *Appl. Phys. Lett.*, vol. 54, no. 26, p. 2707, 1989.
- [33] E. Glaser, J. M. Trombetta, T. A. Kennedy, S. M. Prokes, O. J. Glembocki, K. L. Wang, and C. H. Chern, "Detection of magnetic resonance on photoluminescence from a Si/Si<sub>1-x</sub>Ge<sub>x</sub> strained-layer superlattice," *Phys. Rev. Lett.*, vol. 65, no. 10, p. 1247, 1990.

- [34] L. C. Lenchyshyn, M. L. Thewalt, J. C. Sturm, P. V. Schwartz, E. J. Prinz, N. L. Rowell, J. P. Noel, and D. C. Houghton, "High quantum efficiency photoluminescence from localized excitons in  $\text{Si}_{1-x}\text{Ge}_x$ ," *Appl. Phys. Lett.*, vol. 60, no. 25, p. 3174, 1992.
- [35] T. L. Lin and J. Maserjian, "Novel  $\text{Si}_{1-x}\text{Ge}_x/\text{Si}$  heterojunction internal photoemission long-wavelength infrared detectors," *Appl. Phys. Lett.*, vol. 57, no. 14, p. 1422, 1990.
- [36] G. S. Mitchard and T. C. McGill, "Photoluminescence of Si-rich Si-Ge alloys," *Phys. Rev. B*, vol. 25, no. 8, p. 5351, 1982.
- [37] V. B. Timofeev, "Free many particle electron-hole complexes in an indirect gap semiconductor," *Exciton*, p. 349, 1982.
- [38] J. Sturm, X. Xiao, P. V. Schwartz, C. W. Liu, L. C. Lenchyshyn, and M. Thewalt, "Band-edge exciton luminescence from Si/Strained  $\text{Si}_{1-x}\text{Ge}_x/\text{Si}$  structures," *J. Vac. Sci. Technol.*, vol. B10, no. 4, p. 1998, 1992.
- [39] E. Cohen, M. D. Sturge, M. A. Olmstead, and R. A. Logan, "Electron-hole plasmas in photoexcited indirect-gap  $\text{Al}_{1-x}\text{Ga}_x\text{As}$ ," *Phys. Rev. B*, vol. 22, p. 771, 1980.
- [40] J. Shah, M. Combescot, and A. H. Dayem, "Investigation of exciton-plasma Mott transition in Si," *Phys. Rev. Lett.*, vol. 38, p. 1497, 1977.
- [41] N. F. Mott, *Metal-Insulator Transitions*. Taylor & Francis, 1990.
- [42] X. Xiao, C. W. Liu, J. C. Sturm, L. C. Lenchyshyn, and M. L. Thewalt, "Photoluminescence from electron-hole plasmas confined in  $\text{Si}/\text{Si}_{1-x}\text{Ge}_x/\text{Si}$  quantum wells," *Appl. Phys. Lett.*, vol. 60, no. 14, p. 1720, 1992.

- [43] G. L. Bir and G. E. Pikus, *Symmetry and Strain-Induced Effects in Semiconductors*. John Wiley & Sons, 1974.
- [44] H. Hasegawa, "Theory of cyclotron resonance in strained silicon crystals," *Physical Review*, vol. 129, no. 3, p. 1029, 1963.
- [45] G. Dresselhaus, A. F. Kip, and C. Kittel, "Cyclotron resonance of electrons and holes in silicon and germanium crystals," *Phys. Rev.*, vol. 98, no. 2, p. 368, 1955.
- [46] E. O. Kane, "Energy band structure in p-type germanium and silicon," *J. Phys. Chem. Solids*, vol. 1, p. 82, 1956.
- [47] J. M. Luttinger, "Quantum theory of cyclotron resonance in semiconductors : General theory," *Physical Review*, vol. 102, no. 4, p. 1030, 1956.
- [48] R. Braunstein, "Valence band structure of germanium-silicon alloys," *Physical Review*, vol. 130, no. 3, p. 869, 1963.
- [49] J. C. Hensel and K. Suzuki, "Quantum resonances in the valence bands of germanium II - cyclotron resonances in uniaxially stressed crystals," *Phys. Rev. B*, vol. 9, p. 4219, 1974.
- [50] P. Lawaetz, "Valence-band parameters in cubic semiconductors," *Phys. Rev. B*, vol. 4, no. 10, p. 3460, 1971.
- [51] T. Manku and A. Nathan, "Energy-band structure for strained p-type  $\text{Si}_{1-x}\text{Ge}_x$ ," *Phys. Rev. B*, vol. 43, no. 15, p. 12634, 1991.
- [52] R. Wessel and M. Altarelli, "Analytic solutions of the effective-mass equation in strained  $\text{Si}/\text{Si}_{1-x}\text{Ge}_x$  heterostructures applied to resonant tunneling," *Phys. Rev. B*, vol. 40, no. 18, p. 12457, 1989.
- [53] J. M. Lloyd, *Thermal Imaging Systems*. Plenum Press, 1975.

- [54] F. D. Shepherd Jr. and A. C. Yang, "Silicon schottky retinae for infrared imaging," *IEDM Tech. Digest*, p. 310, 1973.
- [55] J. P. Spratt and R. F. Schwarz, "Metal-silicon schottky diode arrays as infrared vidicon retinae," *IEDM Tech. Digest*, p. 306, 1973.
- [56] F. D. Shepherd Jr., A. C. Yang, S. A. Roosild, J. H. Bloom, B. R. Capone, C. E. Ludington, and R. Taylor, "Silicon schottky barrier monolithic IRTV focal planes," p. 981.
- [57] R. Taylor, L. Skolnik, B. Capone, W. Ewing, F. Shepherd, S. Roosild, B. Cochrun, M. Cantella, J. Klein, and W. Kosonocky, "Improved platinum silicide irccd focal plane," *SPIE Advances in Focal Plane Technology*, vol. 217, p. 103, 1980.
- [58] W. F. Kosonocky, "Review of Schottky-Barrier Imager Technology," *SPIE Proceedings - Infrared Detectors and Focal Plane Arrays*, vol. 1308, p. 2, 1990.
- [59] W. F. Kosonocky and H. Elabd, "Schottky-barrier infrared charge-coupled device focal plane arrays," *SPIE Proceedings Infrared Detectors*, p. 167, 1983.
- [60] R. H. Fowler, "The analysis of photoelectric sensitivity curves for clean metals at various temperatures," *Phys. Rev.*, vol. 38, p. 45, 1931.
- [61] B.-Y. Tsaur, M. M. Weeks, R. Trubiano, P. W. Pellegrini, and T. R. Yew, "IrSi Schottky-Barrier Infrared Detectors with 10 -  $\mu\text{m}$  Cutoff Wavelength," *IEEE Elec. Dev. Lett.*, vol. 9, no. 12, p. 650, 1988.
- [62] B.-Y. Tsaur, C. K. Chen, and B. A. Nechay, "Irsi schottky-barrier infrared detectors with wavelength response beyond 12  $\mu\text{m}$ ," *IEEE Elec. Dev. Lett.*, vol. 11, no. 9, p. 415, 1990.

- [63] H. Kanaya, F. Hasegawa, E. Yamaka, T. Moriyama, and M. Nakajima, "Reduction of the barrier height of silicide/p-Si<sub>1-x</sub>Ge<sub>x</sub> contact for application in an infrared image sensor," *Japanese Journal of Applied Physics*, vol. 28, no. 4, p. L544, 1989.
- [64] E. H. Rhoderick, *Metal-Semiconductor Contacts*. Oxford University Press, 2nd ed., 1988.
- [65] S. P. Murarka, *Silicides for VLSI Applications*. Academic Press, 1983.
- [66] H. K. Liou, X. Wu, U. Gennser, V. P. Kesan, S. S. Iyer, K. N. Tu, and E. S. Yang, "Interfacial reactions and schottky barriers of Pt and Pd on epitaxial Si<sub>1-x</sub>Ge<sub>x</sub> alloys," *Appl. Phys. Lett.*, vol. 60, no. 5, p. 577, 1992.